STRUCTURAL DESIGN OF WING TWIST FOR PITCH CONTROL OF JOINED WING SENSORCRAFT

THESIS

Fred A. Kimler III, Captain, USAF
AFIT/GAE/ENY/06-M20

DEPARTMENT OF THE AIR FORCE
AIR UNIVERSITY

AIR FORCE INSTITUTE OF TECHNOLOGY

Wright-Patterson Air Force Base, Ohio

AFIT/GAE/ENY/06-M20

STRUCTURAL DESIGN OF WING TWIST FOR PITCH CONTROL OF JOINED WING SENSORCRAFT

THESIS

Presented to the Faculty

Department of Aeronautics and Astronautics

Graduate School of Engineering and Management

Air Force Institute of Technology

Air University

Air Education and Training Command

In Partial Fulfillment of the Requirements for the

Degree of Master of Science in Aeronautical Engineering

Fred A. Kimler III, BS

Captain, USAF

March 2006

AFIT/GAE/ENY/06-M20

STRUCTURAL DESIGN OF WING TWIST FOR PITCH CONTROL OF JOINED WING SENSORCRAFT

Fred A. Kimler III, BS
Captain, USAF

Approved:

Robert A. Canfield	15 Mar 06
Dr. Robert A. Canfield (Chairman)	date
Donald L. Kunz	16 Mar 2006
Dr. Donald L. Kunz (Member)	date
Anthony N. Palazotto	15 Mar 06
Dr. Anthony N. Palazotto (Member)	date

AFIT/GAE/ENY/06-M20

Abstract

This research investigated two aspects of the aft wing structure of a joined wing SensorCraft. First, the efficacy of a novel approach for incorporating wing twist for pitch control was analyzed. This design involved adding a spanwise sliding joint into the wing structure at the lower aft spar of the vehicle's aft wing. Second, the joint section where the forward and aft wings connect and form the outboard wing was redesigned and analyzed to improve the load transmission between the wing spars. Using MSC.NASTRAN, linear and non-linear static analyses were performed to examine the efficiency of the wing twist sliding joint and the forces required to achieve sufficient angular deflections for control. MSC.Patran was then used to perform post-processing of the raw data. Several variations of sliding joint location and composite ply angles were conducted. The sliding joint produced marked improvement in angular deflection over the baseline configuration. Surprisingly, however, ply angle did not have a large effect on the resulting deflections. Additional sliding joints incorporated into the wing structure produced no notable improvements in the obtained deflections either. Although the strain induced into the structure by the aft wing twist was on the order of the aerodynamic forces alone, the force required to twist the wing was significantly reduced by adding the slit in all cases. Flutter speed did not differ notably by the addition of the slit into the aft wing, yet some reduction in buckling strength was noted. The redesigned joint planform does appear to recover some of the buckling resistance lost due to the slit.

AFIT/GAE/ENY/06-M20

For my wife and son

Acknowledgements

I sincerely wish to thank my wife and son for all of their patience and understanding during my many long hours and nights at school and away from home. I would also like to extend my thanks and appreciation to my advisor, Dr. Robert Canfield, for his knowledge, experience and understanding of this project and for keeping me going in the right direction. Special appreciation is also due to the students before me whose previous research was so vital to this work becoming a reality. Thanks goes to Maj Vanessa Bond and Capt Cody Rasmussen for their software assistance. Lastly, thanks goes to Dr. Marina Ruggles-Wrenn, Dr. Maxwell Blair and the faculty and staff of the United States Air Force Institute of Technology for their continual support. I am indebted to you all.

Table of Contents

Page

Page

List of Figures

List of Tables

List of Symbols

Symbol	Description
$\{\delta D\}$	Eigenvector
ε	Strain
φ	Angle of Twist per Unit Length
γ	Shear Strain
η	Shear Modulus Ration
λ	Eigenvalue
Λ_{ib}	Inboard Wing Sweep
Λ_{ob}	Outboard Wing Sweep
ν	Poisson's Ratio
ρ	Density; Radius of Gyration
θ	Angle of Twist
σ	Stress
τ	Shear Stress
A	Area
$\overline{A}$	Median Cross-Sectional Area
Aj	Multipoint Constrain Coefficient
AAW	Active Aeroelastic Wing
AFW	Active Flexible Wing
AML	Adaptive Modeling Language
AVTIE	Air Vehicle Technology Integration Environment
[B]	Strain-Displacemnet Matrix
BMI	Bismaleimide
c	Column End Fixity Coefficient
CLAS	Conformal Load-bearing Antenna Structure

c_m . . . . . Joint Chord Length

c_{ra} . . . . . Aft Wing Chord Length

c_{fa} . . . . . Forward Wing Chord Length

d . . . . . Element Nodal Degrees of Freedom

D . . . . . Global Nodal Degrees of Freedom

DOC . . . . . Direct Operating Cost

E . . . . . Modulus of Elasticity

FEM . . . . . Finite Element Model

ft . . . . . Feet

ft/s . . . . . Feet per Second

GPa . . . . . Gigapascals ($1 \cdot 10^9$ Pascals)

GWOT . . . . . Global War on Terrorism

in . . . . . Inches

ISR . . . . . Intellegence, Surveillence and Reconnaissance

J . . . . . Torsional Consant (also Polar Moment of Inertia)

{k} . . . . . Element Stiffness Matrix

[K] . . . . . Global Stiffness Matrix

$[K_\sigma]$ . . . . . Stress Stiffness Matrix

L . . . . . Column Length

lbs . . . . . Pounds Force

m . . . . . Meters

M . . . . . Applied Moment

m/s . . . . . Meters per Second

MPa . . . . . Megapascals ($1 \cdot 10^6$ Pascals)

mph . . . . . Statute Miles per Hour

mm . . . . . Millimeters ($1 \cdot 10^{-3}$ Meters)

MPC . . . . . Multipoint Constraint

N . . . . . Newtons; Element Shape Function

nm . . . . . Nautical Miles

NASA . . . . . National Aeronautics and Space Administration

NASTRAN . . . . . NASA Structural Analysis

p . . . . . Internal Membrane Pressure

q . . . . . Shear Flow

r . . . . . Element Reactions Forces; Radius

R . . . . . Global Reaction Forces

RADAR . . . . . Radio Detection and Ranging

S . . . . . Wing Span; Tensile Force per Unit Length

SL . . . . . Sea Level

S_{ib} . . . . . Inboard Wing Span

S_{ob} . . . . . Outboard Wing Span

t . . . . . Material Thickness

TR . . . . . Torsional Rigidity

{u} . . . . . Element Nodal Displacements

u_j . . . . . Multipoint Constraint Nodal Degrees of Freedom

UAV . . . . . Unmanned Aerial Vehicle

x_{fa} . . . . . Forward-Aft Wing x-Offset

z_{fa} . . . . . Forward-Aft Wing z-Offset

STRUCTURAL DESIGN OF WING TWIST FOR PITCH CONTROL OF JOINED WING SENSORCRAFT

I. Introduction

1.1 Overview

Militaries throughout history have always needed to acquire knowledge of both the battlefield and their enemy. Since the Global War on Terrorism (GWOT) began with the terrorist attacks of September 11, 2001, the United States military has found itself increasingly reliant upon Unmanned Aerial Vehicles (UAV) for its collection of Intelligence, Surveillance and Reconnaissance (ISR) data. UAVs are ideal for the ISR mission due to their ability to loiter over a region for very long periods of time while providing continual data in near real time. The current generation of UAVs, although very capable, suffer from some major disadvantages, however.

One major disadvantage is that they can only see in one direction. Aircraft, such as the RQ-1A *Predator* and RQ-4 *Global Hawk*, were designed around currently available, off the shelf sensors. These ISR sensors must be pointed in a particular direction. Providing adequate coverage of an area, therefore, requires the aircraft to make

multiple passes over it. Also, these aircraft cannot be used for foliage penetration missions. Due to the long wavelengths necessary to penetrate foliage, RADAR arrays must be quite large to generate them. The arrays employed on the *Predator* and *Global Hawk* simply are not large enough.

One solution to these shortcomings fully integrates the RADAR array and the UAV into a single system. The development of Conformal Load Bearing Antenna Structure (CLAS), shown in figure 1.1, now allows the phased array RADAR antenna to double as an integral part of the vehicle's primary structure [26]. Quite naturally, the wing is the best candidate for the use of the CLAS, having the largest planform area of all the aircraft components.

Figure 1.1 CLAS Material Typical Cross Section

It would seem the flying wing would be the obvious choice for this new SensorCraft configuration. Flying wings, however, generally have poor dynamic stability and control characteristics [9: 22-23]. Since precision tracking is a vital part of an ISR platform, this makes them less of a consideration. Also, the use of a single wing would provide good RADAR coverage forward and aft of the aircraft but would still not provide adequate coverage to the sides.

It is these aspects a SensorCraft using a joined wing surpasses conventional configurations. By having a forward and aft wing which join together in a diamond

pattern, as shown in figure 1.2, the array is given a large surface area and sweep angles. These aid in the ability of the array to provide the desired 360° of RADAR coverage. A comparison of a typical RADAR coverage pattern between a flying wing (Figure 1.3) and joined wing (Figure 1.4) are represented below. The joined wing also has the possibility of improving the SensorCraft's gross weight and aerodynamic performance versus other types of planform configurations [46].

Figure 1.2 Joined Wing SensorCraft

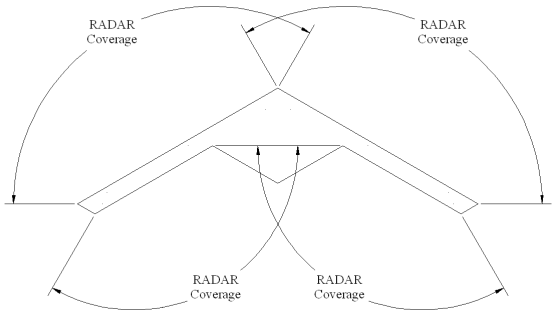

Figure 1.3 Possible RADAR Coverage of a Flying Wing Aircraft

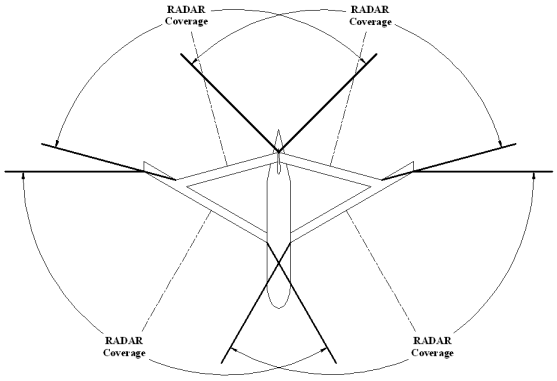

Figure 1.4 Possible RADAR Coverage of a Joined Wing Aircraft

The joined wing SensorCraft, as examined in this research, has a total wingspan of 65 meters and stands about 12 meters in height (see Table 3.1 for a more detailed dimensional overview). It incorporates the CLAS as the upper and lower wing skins of both the forward, inboard wing and the aft wing. A smaller wing is then mounted outboard of the joint where the two inboard wings attach to one another. This wing configuration provides for a 1.50 m x 18.0 m (5.0 ft x 60.0 ft) array to be housed in both the forward and aft wings, as is shown in Figure 1.5. Coupled with proper design of the

phasing electronics, the array will be able to direct its RADAR transmissions over a full 360°.

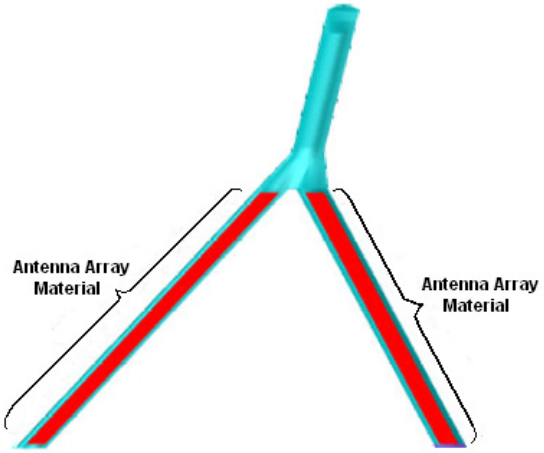

Figure 1.5 Layout of Phased Array Antenna

A major design problem for the joined wing planform involves the vehicle's pitch control. Since a full 360° sensor coverage is desired, use of a conventional elevator design for pitch control would interfere with the RADAR beam propagating aft. Thus an alternate means of providing pitch control is desired in order to prevent this degradation of the signal.

1.2 Research Objectives

The objectives of this research were to examine the effectiveness of using flexible wing twist as a means of providing pitch control to the aircraft and to improve the load paths through the spars in the joint section of the wing. Using wing twist as a means of control has not been used often since the Wright brothers' *Wright Flyer*. The high speeds of modern aircraft make torsionally compliant wings undesirable because of aeroelastic

effects, primarily flutter. The joined wing concept, however, presents the new possibility of reviving this means of control. Since the aft wing mates with the forward wing, it is somewhat constrained against these aeroelastic effects. This allows the development of a torsionally compliant aft wing, through the use of a spanwise slit in the lower wing surface. How great the effect of the slit and the amount of attainable twist are the primary objectives of this research.

1.3 Research Focus

This research focused on the finite element analysis of the structural design in two areas of the joined wing design. The first effort focused on designing and analyzing a realistic and manufactureable design for inducing twist into the aft wing. The second effort involved redesign of the joint section of the wing in order to improve the load paths between the spars of the different wing sections (forward, aft and outboard wings).

1.4 Methodology Overview

The design of the twist mechanism involved three aspects. First, a structural concept was developed. Solid models were then developed to assist the visualization of the developed concept. These models were also beneficial in determining clearances for maintainability and manufacturability of various components. Second, a simplified finite element model was developed in order to analyze the slit concept. Of interest here are the forces necessary to constrain the slit from separating, as well as the overall stresses in the wing. This could be used later for structural component sizing. Finally, several

parameters were altered to note their effects on the design's effectiveness. These parameters were: the number of slits, the end fixity of the aft wing and the ply angles of the carbon plies in the CLAS material.

Lin, Jhou and Stearman have already shown that the fixity of the aft wing can dramatically affect the loads transferred between the forward and aft wings [17]. This study investigates the effects of using different fixities on the aft wing twist capability and loads.

The primary flexibility of designing using composite materials is their inherent capacity for tailoring. By altering the angles of various plies comprising the composite layup, the overall material responses can be adjusted until a suitable solution has been determined.

1.5 Assumptions/Limitations

This research effort is an extension of the work performed by Rasmussen [31]. He developed the baseline finite element model by optimizing the configuration proposed by Roberts [35]. This model was then modified and updated for the purposes herein. The analyses presented here are all static and have, therefore, the limitations associated with all such analyses.

Additional aerodynamic analysis was not performed following the redesign of the joint section. Instead, loads from the original load cases were redistributed from the load distribution over the original joint to the new joint design without recalculating the aerodynamic forces over the new joint section. This redistribution resulted in roughly

two-thirds of the loads from the upper surface of the original joint to be used in the analysis of the new joint. Although this is not very precise, the area affected by the change is relatively small and should not effect the overall results being sought. Finally, no re-optimization of this new joint configuration was performed. As such, some of the stresses and strains may exceed the current material limits.

1.6 Implications

Being able to incorporate into the design a means of pitch control presenting no interference with the sensor arrays solves one of those major hurdles in the usage of the joined wing SensorCraft concept. This research develops a feasible means of producing twist in a wing without an increase in the aircraft's gross weight. Indeed gross weight may possibly decrease due to the lack of a need for multiple actuators and additional control surface structure.

1.7 Outline

The next chapter covers some of the past research efforts of joined wing design. Some of the more recent investigations of this configuration are also introduced here. Finally, the background will be set for this research as well as the particular configuration being studied.

Chapter III discusses the methodology behind the research presented herein. The development of the finite element models (FEM) which were used are presented here. The various configurations and the different aerodynamic and applied loads used in the

analysis are presented also. Torsion in thin walled, open cross-section beams will then be developed, as it serves as the basic physical concept behind this research.

Following this, the results from this research will be discussed in Chapter IV. Finally, Chapter V presents the author's conclusions and recommendations. Some additional results and supporting information is available in the appendices.

II. Literature Review

2.1 Introduction

This chapter presents some past research efforts into the joined wing concept. Also presented here are some of the more recent investigations into various aspects of the joined wing design.

2.2 Joined Wing Structural Design Aspects

The joined wing configuration was first proposed in 1976 by Dr. Julian Wolkovitch under a patent [46] and later expounded upon in a journal article [44] and subsequent patent [45]. In his article, Dr. Wolkovitch made several claims regarding the advantages of this type of aircraft configuration. Primarily, the joined wing offers a lighter structural weight and greater aerodynamic efficiency as compared to an equivalent conventional aircraft configuration. Also of interest is the fact that the plane of bending in the joined wing is inclined, as is shown in figure 2.1.

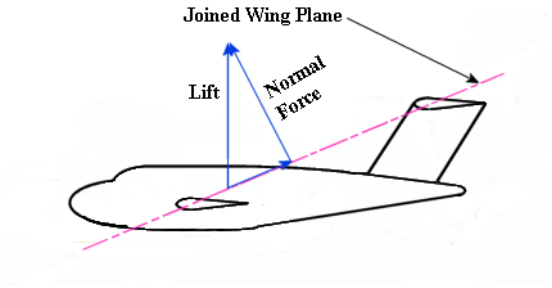

Figure 2.1 Plane of Bending in a Joined Wing

This inclination develops stresses in the wing box that are greatest in the upper, forward spar cap and the lower, aft spar cap of each wing. This is a very different stress contour than is seen in a conventional cantilevered wing aircraft, where the stresses due to the bending are roughly symmetrical. Figure 2.2 below shows how material should then be distributed in both configurations.

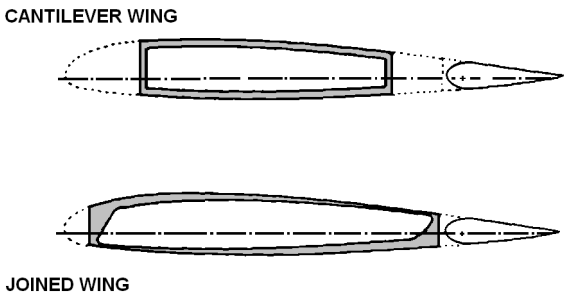

Figure 2.2 Section Thickness Distributions [46]

One of the first analytical studies performed on a joined wing configuration was by Samuels [38]. In this work, Samuels compared a Boeing 727 wing to a joined wing with the same lift and drag performance. She found the joined wing was indeed lighter than a conventional wing. Another study between NASA-Ames Research Center and the University of Texas at Austin examined the effect of different fixativities of the joint between the forward and aft wings [27]. This linear static analysis used a simple finite element model to compare the stresses resulting from the various joint types against experimental data collected from a physical model. It was shown that the lowest stress state resulted from a joint which allowed unconstrained chordwise rotations and vertical translations. A later team conducted an aeroelastic analysis on the same models and

discovered that a fixed joint, i.e. constrained in all directions, had the highest flutter velocity and the joint described above had one of the lowest [17].

It was shown in these early studies that the joined wing was a highly flexible structure. The aft wing, because of its forward and downward sweep, carries a large compressive load. Gallman, Kroo and Smith, therefore, included a buckling analysis in their optimization of a joined wing design [12]. They compared a Douglas Aircraft Company DC-9-30 against a comparable joined wing aircraft. They found that, before buckling was a constraint, the joined wing provided a 2% savings in direct operating cost (DOC) over the conventional aircraft. When, however, buckling was added as a constraint, the joined wing was 3.2% more expensive to operate versus a conventional aircraft.

In a later study by Gallman and Kroo, they examined another joined wing design for the medium transport mission [10]. This research optimized a joined wing using a fully stressed design method, as opposed to the minimum weight methods used in their study above. This approach, again incorporating buckling as a constraint, was only 0.9% heavier than the minimum weight design. This weight savings of the minimum weight joined wing only realized a 0.02% increase in the final DOC. Since this is such a complicated and lengthy method, they concluded the fully stressed design method was more than sufficient as an optimization scheme.

Finally, it should be noted that, in the presentation of their optimization methods, these DOC values were based on a fuel cost of only seventy cents per gallon. Had the fuel cost been $1.40 per gallon, the joined wing would have had a DOC savings of 5-7% over the conventional aircraft [11].

Gallman, Kroo and Smith's work brought attention to several notable design parameters for the joined wing concept. Their research showed the importance of including a buckling analysis. They also noted additional DOC savings over conventional aircraft might be realized by decreasing the static margin of the joined wing. Similarly, they pointed out that close attention should be paid to the maximum lift coefficient attainable by the vehicle, because of the short tail moment arm resulting from the rear wing [16].

In 2001, Livne presented an extensive summary of the work on the joined wing concept prior to that date [18]. He also pointed out the need to incorporate the interface of the aft wing with the vertical stabilizer. Since the aft wing is buckling critical, flexibility of the vertical stabilizer could have a significant effect in the wing's structural dynamics. Because of these complex, coupled interactions between the aerodynamics and structure, he advocated the use of a multidisciplinary approach to the design of joined wing aircraft.

In the mid 1980s, NASA-Langley Research Center and Rockwell International Corporation began a program called the Active Flexible Wing (AFW) [29]. Its purpose was to develop and demonstrate load alleviation and flutter suppression in a highly flexible wing. Use of a flexible wing has the advantages of being significantly lighter structurally and permitting improved aerodynamics during maneuvering. Typically, however, this large flexibility in the wing degrades roll performance and can lower the speed at which flutter or divergence occurs. Control laws were successfully tested which allowed roll maneuvering at 17-26% above the flutter dynamic pressure and reduced roll maneuver loads by up to 50%.

At the conclusion of this program, the US Air Force conducted a similar series of wind tunnel tests using a fifth scale model of the F-16 *Agile Falcon* wing [28]. Most notable from this program was the finding that, as the aileron reversal dynamic pressure was approached, the outboard leading edge slat became more effective in influencing the roll performance. Using a wing model having a 25% less stiff outboard section, tests showed a factor of two to four increase in control power using only the outboard leading edge slat over that of the baseline wing beyond the reversal boundary. By using the flight control system to provide negative deflections of the aileron in concert with actuation of the slat, the control power could be further increased by up to an additional 10%.

Shortly after the conclusion of the *Agile Falcon* wing tests above, NASA took the next logical step in highly aeroelastic wing technology: the Active Aeroelastic Wing (AAW) program. During this program, a NASA F/A-18 had modified pre-production wings installed. Original flight testing of the pre-production F/A-18 showed the aircraft's wings could exhibit aileron reversal within its intended performance envelope [19]. As a result, the pre-production wings were stiffened, as is typical, to prevent reversal from occurring. The NASA modifications returned the wings back to this pre-production stiffness level.

Figure 2.3 NASA Active Aeroelastic Wing Aircraft [7]

Once modifications and ground testing were complete, the aircraft successfully flew a total of eighty-six test flights in two phases [7]. These flights proved the validity of control strategies for aircraft with highly aeroelastic wings. Just as important, several different models for predicting the behavior of the wing and aircraft were created and validated. These models will be quite valuable for highly flexible aircraft such as the joined wing in the future.

2.3 Recent Joined Wing Research

Much of the early work on both conventional and joined wing aircraft had to be simplified by the original authors. This does not necessarily limit the value of the research. Indeed it is still very valuable for showing trends and areas where additional study is necessary. In the past decade, computing technology, computational ability, and software/analytical capability have increased dramatically. This new capacity now allows researchers to do more detailed and complex investigations of the joined wing concept.

An examination of the recent literature shows two relatively distinct tracts of study. Aeroelasticity analysis and structural optimization make up the first tract, with various controls strategies forming the second tract. As mentioned earlier, the highly coupled behavior of the joined wing's structure and aerodynamics requires that any optimization scheme being employed include aeroelastic effects. A number of researchers have, therefore, been investigating these two areas.

Blair and Canfield proposed a means of performing an integrated analyses for a joined wing design [4]. The model they studied was nearly twice the size of that in Gallman and Kroo's research [10]. Blair and Canfield identified three points of interest here. Firstly, they found that the load distribution of the wing changed as the wing deflected, requiring the aircraft to be re-trimmed. Secondly, the outboard wing deformed to a nose down angle of attack for some of the critical buckling modes. Lastly, the model incorporated wing twist as the means of pitch trim, through the use of an actuator in the vertical tail to apply torque to the aft wing. As a result, they noted that large angle of attack changes (or twist) significantly increased the drag produced by the aft wing.

Schwartz, Canfield and Blair demonstrated this process could be successfully applied in a study of effectiveness of a control surface at various locations on the outboard wing of a joined wing UAV [40]. Roberts performed an optimization of this same model, based first on a conventional aluminum structural layout and followed later by a similar composite structure, using nonlinear analysis [36]. Initial nonlinear analysis showed deformations nearly six times greater than indicated by the linear analyses, demonstrating quite clearly the importance of performing a nonlinear analysis. The body of their work has shown that the nonlinear effects of aerodynamic trim could be incorporated within structural optimization to a converged design. Kaloyanova, Ghia and Ghia confirmed these same results in their investigation of a very similar model [15].

By this time, Blair had integrated this process into a user interface known as the Air Vehicle Technology Integration Environment (AVTIE) using the Adaptive Modeling Language (AML). Rasmussen would expand upon his work with AVTIE and make some

additional automation using MATLAB® [31]. In concert with Blair and Canfield, he also presented an excellent study on configuration optimization using response surface analysis techniques [32]. In this manner, the aircraft's configuration and structure were optimized concurrently.

The other area of joined wing study focuses on control strategies for highly flexible wings. These studies have developed directly from NASA's AFW and AAW programs mentioned above. Like these programs, active aeroelastic control employs several control surfaces to create proper aircraft control; whereas, conventional control is usually obtained by the deflection of a single or double control surface, such as an elevator or aileron/leading edge flap.

Raveh, Reich and Zink present a good first cut analysis of a joined wing using these active aeroelastic control techniques [34]. They applied these control schemes to various trim conditions in order to limit the wing deformation from its undeformed shape. They had very good success in keeping the deformed wing shape close to the undeformed state in both steady and maneuvering trim conditions. Bowman, Reich and Sanders took this study further and looked at trim during an entire mission profile [33]. Again, the results were very effective.

In addition to the modification of existing control surfaces via an active control system, others have been researching the use of piezoelectric materials. These materials induce strains when an electric current is applied to them. By imbedding these materials into more conventional composite materials, they act as an anisotropic piezocomposite actuator. Brown and Cesnik examined how effective these might be in a joined wing

versus a conventional aileron [6]. Unfortunately, the aileron configuration had much better roll performance than the piezocomposite by about a factor of 3.75. They point out, however, that the materials research into these materials is advancing rapidly and may develop to within this range in the foreseeable future.

2.4 Basis for Current Research

This research expands upon the work of Roberts [36] and Rasmussen [31]. The aircraft developed by these two has finally reached a level of design maturity where the first detailed design steps can now be undertaken. Thus far in the literature, numerous conceptual design and optimization studies have been completed on various joined wing configurations; however, as yet there have been few studies of the more detailed aspects of a joined wing aircraft. This research will develop a physical means to effect pitch control for the aircraft by using wing twist induced into the aft wing by means of an applied actuator load. Complicating this task is the highly stiff nature of modern composite aerostructures (as will be explained in Chapter III). This excess stiffness requires the development of a means of globally reducing the torsional resistance of the aft wing structure. Also, these tasks must be accomplished by a means that can be manufactured and in a manner that is not weight-restrictive.

III. Methodology

3.1 Introduction

This chapter describes some of the methodologies behind the research presented. The aircraft under study will be described followed by discussions on the loads and materials being used in the modeling of the aircraft. This will be followed by details of some of the theory behind the analyses being conducted. Finally, the physical and analytical models of the spanwise slit will be described.

3.2 Aircraft Configuration

As defined earlier, the joined wing is an aircraft similar to a tandem wing aircraft; however, the forward and aft wings join together at some outboard location on the planform. The wing being studied herein is a rather large aircraft, having a wingspan of some 65 m (215 ft). The vertical separation between the forward and aft wings is 7 m (23 ft). These dimensions give the SensorCraft a footprint comparable to a Boeing 747 [5]. Figure 3.1 below shows some of the important dimensions of the SensorCraft under study. The values of these dimensions are given in Table 3.1. Figure 3.2 shows a view of the finite element model of the wing planform.

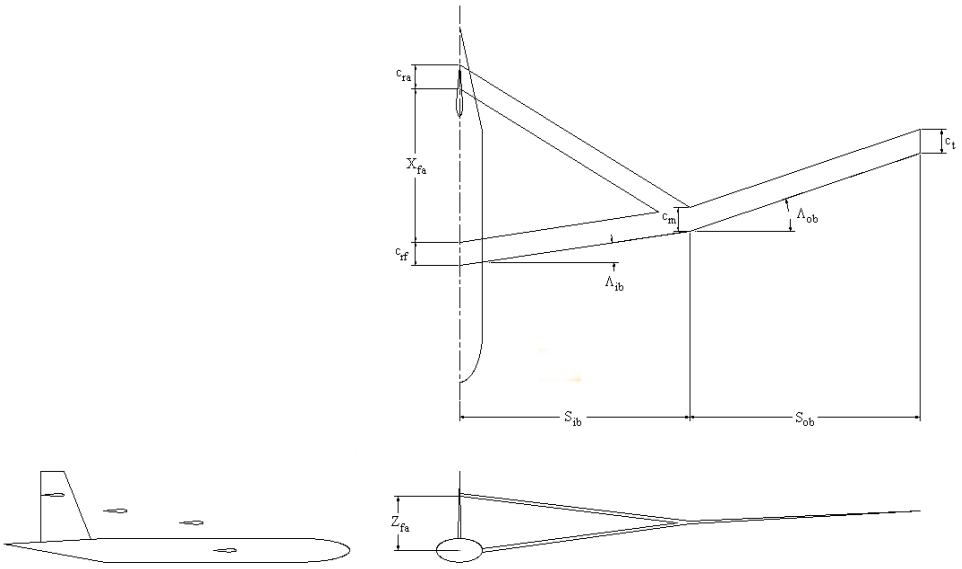

Figure 3.1 SensorCraft Configuration

Table 3.1 SensorCraft Dimensions

Parameter	Symbol	Value
Wing Tip Chord Length	c_t	2.5 m (8.2 ft)
Aft Wing Chord Length	c_{ra}	2.5 m (8.2 ft)
Forward Wing Chord Length	c_{rf}	2.5 m (8.2 ft)
Joint Chord Length	c_m	5.0 m (16.5 ft)
Inboard Wing Sweep Angle	Λ_{ib}	30°
Outboard Wing Sweep Angle	Λ_{ob}	30°
Inboard Wing Span	S_{ib}	26.0 m (85.3 ft)
Outboard Wing Span	S_{ob}	8.0 m (26.4 ft)
Forward-Aft Wing x-Offset	x_{fa}	19.5 m (64.4 ft)
Forward-Aft Wing z-Offset	z_{fa}	7.0 m (23.1ft)

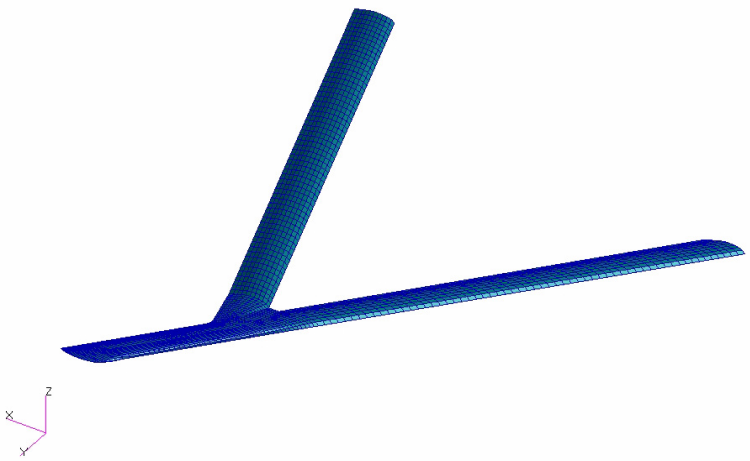

Figure 3.2 SensorCraft Wing Finite Element Model

3.3 Mission Profile

The mission of an ISR platform is to provide information considered valuable to the platform's owners. Often, the gathering of ISR information requires the platform to provide long term coverage of a particular area of interest in order that any movement or changes in the area may be noted and passed along. The introduction of UAV technology has revolutionized this capability. Previously, ISR platforms consisted of manned aircraft, such as the U-2 *Dragon Lady*, or satellites. Manned aircraft are limited by the onset of pilot fatigue; whereas, satellites suffer from the predictability of their orbits. The UAV is, in theory, only limited by the amount of onboard fuel.

For the SensorCraft, this capability is exploited by developing a mission profile specifying an endurance time over the target area of 30-48 hours. The full mission profile is described by Figure 3.3. As can be seen in the figure, the SensorCraft also takes advantage of high altitudes. This helps to mask the aircraft's visual and aural signatures, without detrimentally affecting the performance of the onboard sensor equipment [3].

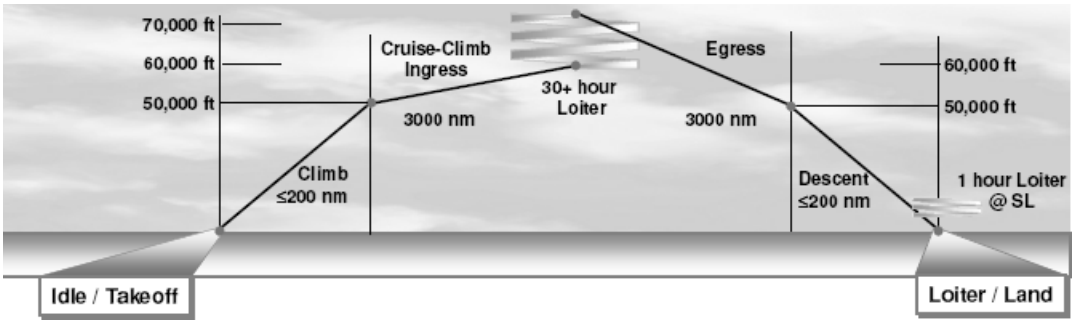

Figure 3.3 SensorCraft Mission Profile [20]

3.4 Load Cases

In his study of the SensorCraft, Roberts identified four critical load cases during the above mission profile [36]. The first is a 2.5g maneuver while the aircraft is still full of fuel. The second case is the same 2.5g maneuver while the aircraft is nearly empty of fuel. The third load case represents a turbulent gust being encountered during 1.0g cruise flight while the aircraft is nearly empty of fuel. The final case represents the severe case when the aircraft is forced to return for a landing shortly after takeoff. It becomes a case of a 1.75g impact with the runway while a full fuel load is onboard.

3.5 Materials

The wings of the SensorCraft are made entirely of advanced composite materials. The use of composite materials developed from the desire to prevent any possible attenuation of the RADAR signal from the array that may occur from the use of conventional metallic materials. Composites are known as orthotropic materials, since their mechanical properties differ depending upon from which direction the loads are applied. They are very strong in the direction of the fiber, but tend to be very weak in the matrix direction by comparison. Use of this behavior can be made by orienting the fibers in the directions requiring the most strength.

This same mechanical behavior also complicates the analysis of structures made from composite materials. Instead of being able to calculate stresses and strains directly, as one would for an isotropic material like aluminum, numerous different mechanical properties must first be known. Only then can the stresses and strains be calculated through the use of a compliance matrix of these properties. Equation (3.1) shows the familiar Hooke's Law used to calculate stress or strain for an isotropic material; whereas, Equation (3.2) shows what is necessary to calculate these same stress and strain values for an orthotropic material [2: 66]. In these equations, the following definitions are made:

Table 3.2 Mechanical Property Definitions

Symbol	Property
E	Young's Modulus
G	Shear Modulus
ε	Strain
γ	Shear Strain

Table 3.2 (Continued) Mechanical Property Definitions

Symbol	Property
ν	Poisson's Ratio
σ	Stress
τ	Shear stress

$$\{\sigma\} = [E]\{\varepsilon\} \tag{3.1}$$

$$\begin{bmatrix} \varepsilon_1 \\ \varepsilon_2 \\ \gamma_{12} \end{bmatrix} = \begin{bmatrix} \frac{1}{E_1} & -\frac{\nu_{21}}{E_2} & 0 \\ -\frac{\nu_{12}}{E_1} & \frac{1}{E_2} & 0 \\ 0 & 0 & \frac{1}{G_{12}} \end{bmatrix} \begin{bmatrix} \sigma_1 \\ \sigma_2 \\ \tau_{12} \end{bmatrix} \tag{3.2}$$

One drawback, aside from the cost of composite materials, is the dependence of the mechanical properties of a particular composite laminate upon the manufacturing and curing processes being employed. These factors affect the fiber to matrix volume ratio and void percentage of the layup, in turn directly affecting the final strength of the layup. As such, there are no standard mechanical property tables for composite materials like there are for isotropic materials. This makes it very difficult for a designer to choose a specific material to use in the analysis. The following descriptions of the materials used on the SensorCraft have been developed using a combination of supplier data sheets, published test results and predictive techniques.

Where possible, the data from the material manufacturer or supplier has been used. These data typically supply only the tensile and shear strengths in the major directions. Where properties were absent from the manufacturer, such as shear modulus for example (one commonly not supplied), predictive techniques were used to determine the

properties. One such technique, shown by Equations (3.3) and (3.4), is based on a modified rule of mixtures approach [13: 395-401].

$$\frac{1}{E_{11}} = \frac{1}{\nu_f + \eta_1 \nu_m}\left(\frac{\nu_f}{G_f} + \frac{\eta_1 \nu_m}{G_m}\right) \tag{3.3}$$

$$\frac{1}{E_{22}} = \frac{1}{\nu_f + \eta_2 \nu_m}\left(\frac{\nu_f}{E_f} + \frac{\eta_2 \nu_m}{E_m}\right) \tag{3.4}$$

where:

$$\eta_1 = \frac{1}{2}\left(1 + \frac{G_m}{G_f}\right) \tag{3.5}$$

$$\eta_2 = \frac{1}{2}\left(1 + \frac{E_m}{E_f}\right) \tag{3.6}$$

E_{11}, E_{22}: Young's Modulus in 1 and 2 directions, respectively
G_f, G_m: Shear Modulus in fiber and matrix directions, respectively
ν_f, ν_m: Poisson's Ratio in fiber and matrix directions, respectively

If no useful supplier data either could be found or were too sparse to effectively use predictive techniques, values for typical properties were used.

The leading and trailing edges are constructed of a Kevlar-49® plain weave fabric and epoxy matrix laminate. Kevlar was chosen primarily for its impact resistance, since its load carrying capacity was less of a constraint. Table 3.3 shows the properties of the Kevlar-49®/DuPont 924 unidirectional aramid/epoxy prepreg being used in the finite element model.

Table 3.3 Mechanical Properties of Kevlar-49®/DuPont 924 [30]

Property	Value
E_{11}	72.0 GPa
E_{22}	5.0 GPa
ν_{12}	0.41
G_{12}	2.0 GPa
G_{13}	2.0 GPa
G_{23}	2.0 GPa
Density, ρ	1.38 g/cm^3

The CLAS material is composed of several different materials, as was shown in Figure 1.1. The exact materials used in the construction of the CLAS is proprietary to Northrop Grumman Corporation and had to be estimated for this analysis [26]. The quartz layer of the CLAS was modeled as an Astroquartz II® satin weave fabric and F650 bismaleimide (BMI) resin laminate. Its mechanical properties are shown in Table 3.4. The carbon foam core material was modeled as Touchstone Research Laboratory, Inc. *CFOAM 25* [43]. Table 3.5 shows its mechanical properties.

In addition to the CLAS, the wing spars are made from a carbon fiber and epoxy matrix laminate. Since these elements are the primary load-bearing structure for the aircraft, a high tensile strength fiber needed to be combined with a resilient matrix. To meet these requirements, a combination of HexPly® 8551-7, a toughened epoxy resin matrix, and IM-7, an intermediate modulus 12k tow carbon fiber. The mechanical properties of IM-7/8551-7 are shown in Table 3.6 [14].

Table 3.4 Mechanical Properties of Astroquartz II®/F650 [14]

Property	Value
E_{11}	26.9 GPa
E_{22}	26.89 GPa
ν_{12}	0.19
G_{12}	5.0 GPa
G_{13}	60.7 MPa
G_{23}	60.7 MPa
Density, ρ	1.78 g/cm^3

Table 3.5 Mechanical Properties of CFOAM 25® [43]

Property	Value
E	830.0 MPa
G	587.0 MPa
ν	0.29
Density, ρ	400.0 kg/m^3

Table 3.6 Mechanical Properties of IM-7/8551-7 Carbon/Epoxy

Property	Value
E_{11}	158.6 GPa
E_{22}	9.3 GPa
ν_{12}	0.30
G_{12}	6.0 GPa
G_{13}	5.0 GPa

Table 3.6 (Continued) Mechanical Properties of IM-7/8551-7 Carbon/Epoxy

Property	Value
G_{23}	3.0 GPa
Density, ρ	1.272 g/cm^3

3.6 Linear Finite Element Statics Theory

Linear statics encompasses an analysis of a structure in static equilibrium, i.e. the absence of accelerations. Two key assumptions are also made in a linear analysis: small displacements and small rotations. The finite element method then discretizes the structure into discrete elements connected at points called nodes. Each element can then be assembled into the equation: $[k]\{d\} = \{r\}$, where $[k]$ is the element stiffness matrix, $\{d\}$ is a vector of the nodal degrees of freedom, and $\{r\}$ is the vector of reaction forces on the element [8].

The individual structural elements can then be assembled into a system of these linear equations through the use of a matrix of nodal connectivity describing the relationships of the nodes of one element to another. The equation becomes: $[K]\{D\} = \{R\}$, where $[K]$ is the structure or global stiffness matrix, $\{D\}$ is the global nodal degrees of freedom, and $\{R\}$ is the global reaction forces.

The nodal displacements, $\{u\}$, can be found from: $\{u\} = [N]\{d\}$, where $[N]$ is a matrix of element shape functions. The shape functions are dependent upon the type of elements being used in the analysis. Similarly, strain may be found using: $\{\varepsilon\} = [B]\{d\}$, where the strain-displacement matrix, $[B] = [\partial][N]$. Stress can be

calculated using the equation: $\{\sigma\} = [E]\{\varepsilon\}$, where $[E]$ is the constitutive matrix of elastic moduli. The constitutive matrix is especially convenient for composite materials having different moduli in different directions.

The element stiffness matrices as defined above can work for planar (2D) or volumetric (3D) elements. An alternative method for developing it is through the use of Equation (3.7) for a planar element or Equation (3.8) for a volumetric element.

$$[k] = \iint_A [B]^T [E][B] dA \tag{3.7}$$

$$[k] = \iiint_V [B]^T [E][B] dV \tag{3.8}$$

3.7 NASTRAN Buckling Theory

Buckling refers to a phenomenon where a structure subjected to a load will undergo much larger deflections than expected from linear theory due to a very small increase in the applied load. So long as this critical load is not exceeded too much, the material will not fracture or separate. This type of buckling is also known as bifurcation buckling. This name comes from the nature of the buckling phenomenon whereby two infinitesimally close shapes, unbuckled and buckled, may be possible at the same load value.

Adding to the buckling problem is another phenomenon called stress stiffening. This refers to the reduction of an element's resistance to bending due to the influence of compressive membrane forces and their associated stresses. Thus, in addition to the

normal stiffness matrix, a new stress stiffness matrix, $[K_\sigma]$, must be taken into account in order to solve a buckling problem. This stress stiffness matrix is determined from Equation (3.9).

$$[K_\sigma] = \iiint_V [G]^T \begin{bmatrix} s & 0 & 0 \\ 0 & s & 0 \\ 0 & 0 & s \end{bmatrix} [G] dV \tag{3.9}$$

where:

$$[G] = [\partial][N] \tag{3.10}$$

and

$$[s] = \begin{bmatrix} \sigma_x & \tau_{xy} & \tau_{xz} \\ \tau_{xy} & \sigma_y & \tau_{yz} \\ \tau_{xz} & \tau_{yz} & \sigma_z \end{bmatrix} \tag{3.11}$$

After the stress stiffness matrix has been determined, the buckling eigenvalue problem can be set up and solved. Equation (3.12) shows the buckling eigenvalue problem, where λ is the eigenvalue and $\{\delta D\}$ is the associated eigenvector. The eigenvalue amounts to the load factor that, when multiplied by the applied load, results in the critical buckling load. The eigenvector is the actual buckling mode shape, representing the nodal displacements at the buckling load. This eigenvector provides only shape information, however, and not the actual magnitudes of the nodal displacements at the critical load.

$$([K] + \lambda[K_\sigma])[\delta D] = \{0\} \tag{3.12}$$

Solution of Equation (3.12) often leads to several eigenvalues being determined. From the structures standpoint, only the lowest value is usually of interest, since it would result in the lowest critical load.

Another factor affecting the magnitude of the critical buckling load is the end fixity of the column under consideration. For example, a column with both ends pinned buckles at a much lower critical load than does a column with both ends fixed. Often the end fixity effect is applied as a coefficient to the standard Euler buckling equation, Equation 3.13. Values for the end fixity coefficient, *c*, are shown in Figure 3.4 below.

$$P_c = \frac{c\pi^2 E}{\left(\frac{L}{\rho}\right)^2} \tag{3.13}$$

where:

E: Young's Modulus
c: End Fixity Coefficient
L: Column Length
ρ: Section Radius of Gyration

Column Shape and End Condition		End Fixity Coefficient	Column Shape and End Condition		End Fixity Coefficient
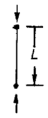	Uniform column, axially loaded, pinned ends	$c = 1$ $\frac{1}{\sqrt{c}} = 1$		Uniform column, distributed axial load, one end fixed, one end free	$c = 0.794$ $\frac{1}{\sqrt{c}} = 1.12$
	Uniform column, axially loaded, fixed ends	$c = 4$ $\frac{1}{\sqrt{c}} = 0.50$	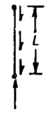	Uniform column, distribution axial load, pinned ends	$c = 1.87$ $\frac{1}{\sqrt{c}} = 0.732$
	Uniform column, axially loaded, one end fixed, one end pinned	$c = 2.05$ $\frac{1}{\sqrt{c}} = 0.70$		Uniform column, distributed axial load, fixed ends	$c = 7.5$ $\frac{1}{\sqrt{c}} = 0.365$
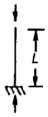	Uniform column, axially loaded, one end fixed, one end free	$c = 0.25$ $\frac{1}{\sqrt{c}} = 2$		Uniform column, distributed axial load, one end fixed, one end pinned	$c = 3.55$ (approx.) $\frac{1}{\sqrt{c}} = 0.530$

Figure 3.4 End Fixity Coefficients for Column Buckling [37]

3.8 Nonlinear Finite Element Theory

Nonlinearity may enter into the structural analysis in one or more of the following three areas: material nonlinearity, contact nonlinearity and geometric nonlinearity [8]. Material nonlinearity can develop once a material has exceeded its yield point. Contact nonlinearity occurs when there is a gap between two elements that may open or close or as a result of nonlinear forces such as friction. Geometric nonlinearity results from violation of the small rotations assumption or changes in load direction during changes in load magnitude.

As a result, the linear equation from Section 3.6 now has both $[K]$ and $\{R\}$ dependent upon $\{D\}$. An iterative process is, therefore, necessary in order to solve for

$\{D\}$, such that $[K]\{D\} = \{R\}$. Further complicating the solution are corrections which must be made to the stiffness matrix. From the buckling discussion, a correction for stress stiffening has been defined, but a correction for the large rotations must now be found.

The process begins by selectively populating an additive strain-displacement matrix composed of linear and nonlinear matrices: $[\tilde{B}] = [B_L] + [B_N]$ [39]. This new strain-displacement matrix is then used to calculate a tangent stiffness matrix that accounts for the large rotation effects. The tangent stiffness matrix is defined by Equation (3.14). The new global stiffness matrix can be found by adding the three different stiffness matrices together: $[\tilde{K}] = [K] + [K_\sigma] + [K_R]$. The iteration procedure can then be started in order to solve for the differential internal forces: $\{dF\} = [\tilde{K}]\{du\}$.

$$[K_R] = \iiint_V \{[B_L]^T[N][B_N] + [B_N]^T[N][B_N] + [B_N]^T[N][B_L]\}dV \tag{3.14}$$

3.9 Torsion in Thin Walled Hollow Sections

A moment, *M*, applied to a cross-section, through the action of an applied torque or couple, induces shear stresses along the perimeter of the section. For closed, thin-walled sections, one technique for determining the shear stress, as well as the resultant twist, is shear flow. Defining $\overline{A}$ as the area of the cross-section as measured from the median lines (see Figure 3.5), the shear flow is given by Equation (3.15) [1].

$$q = \frac{M}{2\overline{A}} \tag{3.15}$$

The shear stress is then:

$$\tau = \frac{q}{t} \tag{3.16}$$

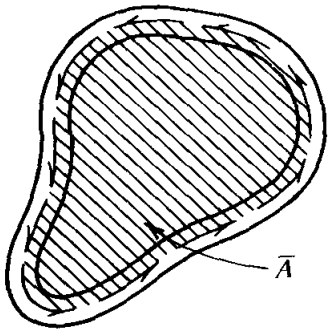

Figure 3.5 Medial Cross-Sectional Area [1:195]

The twist angle due to the torsion is then given by:

$$\theta = \frac{1}{2\bar{A}} \oint_S \frac{q}{Gt} ds \tag{3.17}$$

where G is the shear modulus of the cross-section's material.

By further defining the torsional constant, J (also called the polar moment of inertia for circular cross-sections), as:

$$J = \frac{4\bar{A}^2}{\oint_S \frac{1}{t} ds} \tag{3.18}$$

Equation (3.17) can be re-cast into:

$$\theta = \frac{M}{GJ} \tag{3.19}$$

Another useful parameter is the torsional rigidity, *TR*. The torsional rigidity of a cross-section, defined by Equation (3.20), is dependent upon only the material shape of the cross-section.

$$TR = \frac{M}{\theta} = GJ \tag{3.20}$$

Invariably in aircraft structures, members with open cross-sections, such as angles, channels and tees, are frequently encountered. Attempting to use shear flow can become quite cumbersome for these types of open cross-sections, since the shear flow analogy cannot be applied directly without making several simplifying assumptions (such as Euler-Bernoulli behavior). Simple experiments using a cardboard tube readily show a reduction in the torsional rigidity in open sections versus closed sections under the same applied torque.

In order to quantify the magnitude of this reduction in the torsional rigidity in a more convenient method, use will be made of the elastic membrane analogy. This analogy was first proposed by Barré St. Venant and later expanded upon by Ludwig Prandtl [41]. St. Venant noted the differential equation of the torsion stress function (Equation (3.21)) was proportional to that of a thin elastic membrane, often referred to as a soap film (Equation (3.22)). The two equations also have the same boundary conditions at the edges of the surfaces, namely: $\varphi = z = 0$. The physical interpretation of the elastic membrane analogy is shown in Figure 3.6.

$$\frac{\partial^2 \varphi}{\partial x^2} + \frac{\partial^2 \varphi}{\partial y^2} = -2G\theta \tag{3.21}$$

$$\frac{\partial^2 z}{\partial x^2} + \frac{\partial^2 z}{\partial y^2} = -\frac{p}{S} \tag{3.22}$$

where:

φ:	twist angle per unit length
p:	internal pressure of the membrane
S:	tensile force per unit length of the membrane

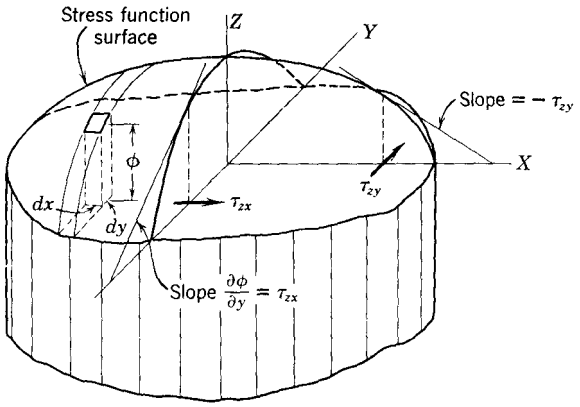

Figure 3.6 Elastic Membrane Analogy of Torsion Stress Function [41]

It was known for the membrane that the slopes in the x- and y-directions are proportional to the stresses in the y- and x-directions, respectively. Also, the volume enclosed by the membrane, $\iint z dx dy$, is proportional to one-half of the twisting moment exerted by the membrane [41]. Given the analogy between Equations (3.21) and (3.22), these same statements must also hold true for the torsion stress function. The results are as follows:

$$\frac{\partial \varphi}{\partial x} = -\tau_{yz} \tag{3.23}$$

$$\frac{\partial \varphi}{\partial y} = \tau_{xz} \tag{3.24}$$

$$\iint \varphi dx dy = \frac{M}{2} \tag{3.25}$$

Along the boundary of the cross-section, the shear stresses must be equal to zero. As an edge is approached, this requires the shear stresses to decrease from some maximum value at the centerline of the section thickness in order to satisfy this boundary condition. Since there exists a discontinuity at the edges of the opening, the shear stresses must approach zero here also. The stress function surface now resembles the same of a membrane over a rectangular surface, as is shown in Figure 3.7. The solution of the torsion stress function for an open cross-section is, therefore, identical to that of a long, thin, solid cross-section.

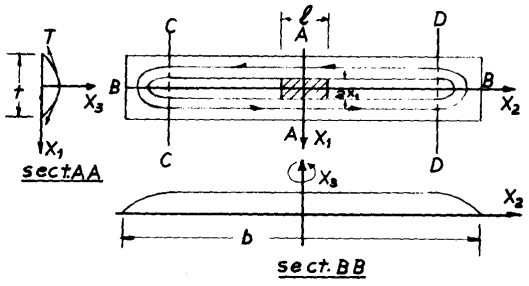

Figure 3.7 Elastic Membrane Over Rectangle [37]

To highlight the differences in torsional rigidity of an open cross-section versus a hollow, closed cross-section, consider the case of a hollow, circular tube. This closed tube undergoes an amount of twist as shown in Equation (3.26) below. Adding a longitudinal slit in the tube results in the twist increasing, as is shown by Equation (3.27). Given that $t \ll r$, the resulting torsional rigidity of the open cross-section could be significantly less than that of the closed cross-section for the same applied moment. Unfortunately, this

decrease in rigidity comes at a cost of higher resultant shear stresses for a given applied moment, as is shown by Equations (3.28) and (3.29). If, however, the same magnitude of stress is sought, a reduction in torsional rigidity results in a lower applied torque being necessary.

$$\theta_{closed} = \frac{1}{2\pi r^3 t} \cdot \frac{M}{G} \tag{3.26}$$

$$\theta_{open} = \frac{3r^2}{t^2} \cdot \frac{1}{2\pi r^3 t} \cdot \frac{M}{G} \tag{3.27}$$

$$\tau_{closed} = \frac{M}{2\pi r^2 t} \tag{3.28}$$

$$\tau_{open} = \frac{3r}{t} \cdot \frac{M}{2\pi r^2 t} \tag{3.29}$$

This is the primary impetus driving this research. By designing for the same amount of strain, the reduction of the torsional rigidity of the aft wing cross-section decreases the magnitude of the moment required to twist the wing compared to the original structure.

3.10 Slit Design and Modeling

The key focus of this research is the development of a means of effecting significant twist into the aft wing which is sufficient to provide adequate pitch control of the aircraft throughout its flight regime. Since the design of most modern aerospace vehicles uses stressed skin wing box concepts, the wings tend to be very stiff. This is due primarily to the wing skins providing significant bending and shear stress resistance

(which is what they are designed to do). A strategy of simply applying a large torque to an unmodified wing would almost certainly exceed the factors of safety of the skins.

The use of conventional control surfaces is problematic also for several reasons. First, the inclined bending plane pointed out by Wolkovitch creates added benefits from pushing the spars as far as possible to the leading and trailing edges of the wing section. This leaves little chord length left for the addition of a control surface. Second, any deflection of a control surface near the antenna array, that happens to be the majority of the wing area already, is likely to cause adverse attenuation of the RADAR signal from the antenna. Another factor complicating the use of conventional surfaces is the large deformation of the wing during flight. In order to avoid binding or locking of the control surfaces, numerous smaller control surfaces would be necessary to prevent excess deformation in the hinge lines of the surfaces. The addition of additional surfaces necessitates the addition of extra actuators, wiring and hydraulics to power them. As a matter of course, this amounts to increases in the vehicle weight, as well as the consequential decrease in payload and range.

In order to maintain the load bearing capability of the wing while reducing the torsional rigidity of the wing section, a spanwise slit was incorporated into the wing structure. By keeping the dimensions of the slit small, it was hoped the incurred shear stress increase would be manageable without a notable weight increase.

The slit is located on the lower surface of the aft wing, just forward of the aft spar. The lower surface was chosen to provide a means of escape for any liquid (water or fuel) which may become trapped inside the wing box. The aft spar was chosen since it generally carries a lesser load than the forward spar.

Modeling of the slit in the finite element model was relatively simple. By placing two sets of nodes at identical positions on the spar line, the elements from the lower skin could be assigned to one set of nodes, and the elements of the spar assigned to the other set. The displacements of the nodes were then related to one another through the use of a multipoint constraint, MPC, bulk data card. The MPC allows an independent node to be mathematically related to one or more dependent nodes. This relationship is defined according to Equation (3.30)

$$\sum_i A_j u_j = 0 \tag{3.30}$$

where:

A_j: coefficient
u_j: nodal degree of freedom

The next step in modeling the gap was to define this relationship between the nodes on either side of the gap. By inspection, it can be seen the gap must be restrained from separating apart vertically from one another. Also by inspection, it can be seen there should be freedom to displace spanwise, since it is the natural tendency for the cross-section to do so as it warps under the torsion load. Optimally, displacements in the spanwise direction should be restrained also; however, doing so would require incorporation of some type of linear slide mechanism. All concepts for this were quite heavy, especially in comparison to leaving it unconstrained.

Thus, the problem becomes one of simply constraining the nodes on either side of the slit to having zero normal displacement between them. Recasting Equation (3.30) gives:

$$\sum_{i}(1)\cdot u_{3_{spar}} + \sum_{i}(-1)\cdot u_{3_{skin}} = 0 \tag{3.31}$$

where:

$u_{3_{spar}}$: vertical displacement of node assigned to the spar element

$u_{3_{skin}}$: vertical displacement of node assigned to the skin element

Somewhat more problematic was the development of a physical and manufactureable model of the slit. Fortunately, being constrained in only the vertical direction substantially simplified the problem. The final design, shown in Figure 3.8, consists of the lower skin resting on top of the lower flange of the aft spar. A stop block, made from a carbon/epoxy laminate and attached to the spar web, sandwiches the skin between it and the flange. Use of nylon or phenolic wear pads attached to the faying surfaces would reduce the friction between them. This would also be beneficial from a maintainability standpoint as well, allowing for the pads to be periodically changed once established wear limits had been exceeded.

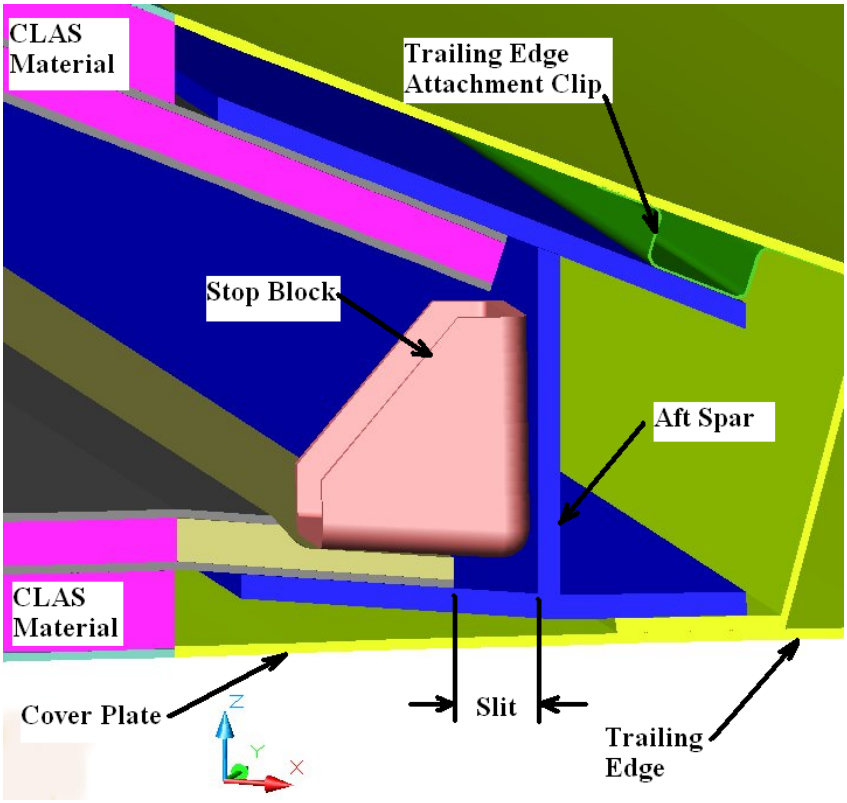

Figure 3.8 Physical Model of Aft Wing Spanwise Slit

3.11 Joined Wing Finite Element Model

The finite element model (FEM) was created to investigate the effects of various loading conditions and optimization schemes on the major structural elements of a joined wing sensorcraft. Figure 3.9 shows a general view of the right half wing model. Overall the model is of a two spar, stressed skin wing box design, as is shown in Figure 3.10. The spars are located at 10% and 80% of the chord length with ribs stationed approximately every meter. Due to the need to permit the lower skin to translate both chordwise and spanwise, the ribs in the aft wing were not attached to the lower CLAS skin. Figure 3.11

shows a view to demonstrate this design. The lower CLAS skin would be reinforced with integral stiffeners bonded in the chordwise and spanwise directions, though these are not present in the FEM.

The finite elements were composed of laminated composite materials, as was described in Section 3.5. The modeling of the laminates was accomplished in NASTRAN by first defining the material properties with either a MAT1 (isotropic) or MAT8 (orthotropic) bulk data entry [23]. Next the laminate was built up with a PCOMP bulk data entry. The PCOMP card allows each ply to be assigned a material, ply thickness and and orientation. Finally, the quadrilateral and triangular elements could then be created, referencing the PCOMP cards.

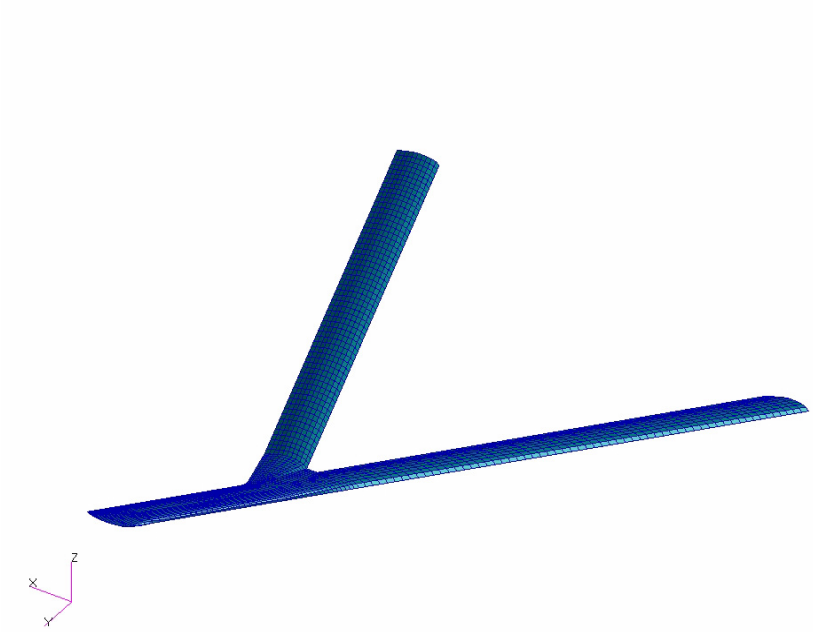

Figure 3.9 Joined Wing Finite Element Model

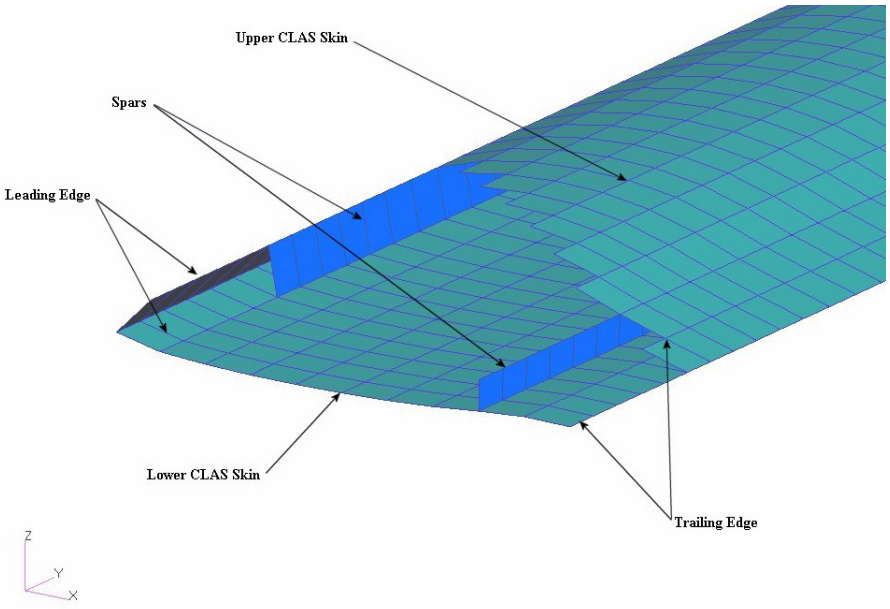

Figure 3.10 Finite Element Model Cutaway View

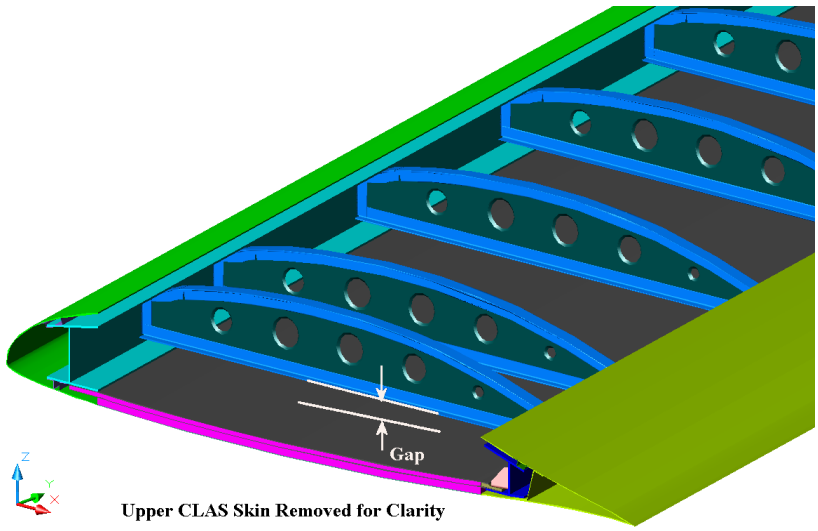

Figure 3.11 Aft Wing Structural Cutaway View

During the initial phases of the analyses, the wing ribs in the aft wing were removed, since they would have prevented the lower skin from moving in the configuration with the slit. In the later analyses, new configurations (#3-5) had the

original ribs added back into the FEM. These ribs were then modified such that the lower edge of the ribs did not attach to the lower skin (see Figure 3.11 above). They remained attached to the upper skin and both spars. The elements comprising the ribs was the identical carbon/epoxy laminates used by Rasmussen and Roberts [31, 35].

3.12 New Joint Design

Initial results indicated high strains being developed due the twist moment being applied, as will be expounded upon more later. For this reason, and to explore other types of joint fixity configurations, a new joint section was designed. The previous model, shown in Figure 3.12, had a joint section in which the spars from each of the wing panels, forward, aft and outboard, were discontinuous with one another. The new design moved the aft wing intersection with the joint forward and up from the original trailing edge position, thereby allowing the forward and outboard wing spars to be continuous through the joint section. The aft wing spars then intersected these spars at the middle of the joint, as is shown by Figure 3.13.

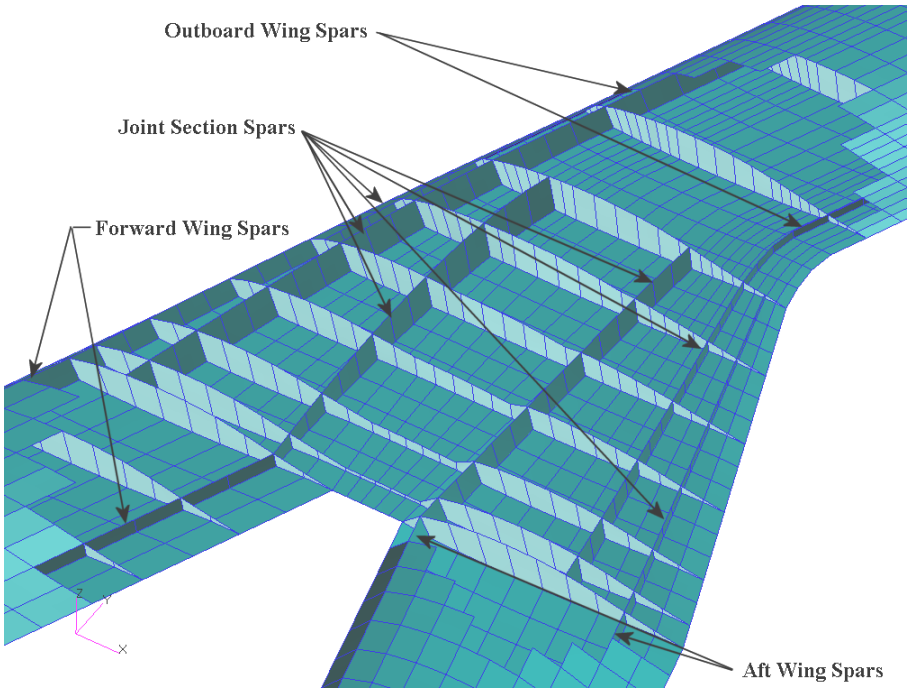

Figure 3.12 Original Joint Configuration Cutaway View

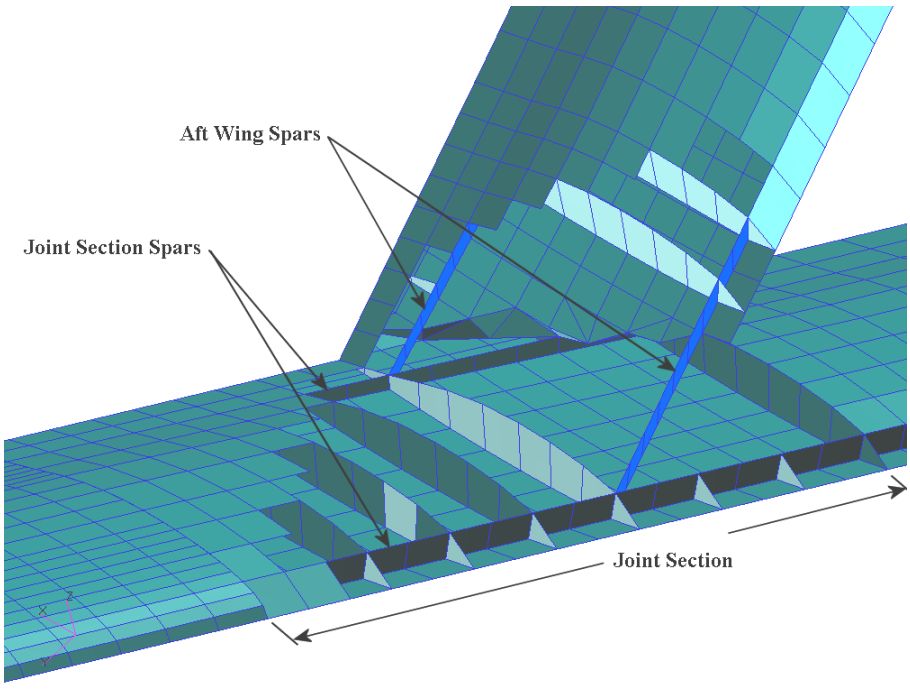

Figure 3.13 New Joint Configuration Cutaway View

3.13 Boundary Conditions and Configuration Control

This research looked into the effects of several loading conditions on several different aft wing configurations to identify the most of feasible means of wing twist. A total of nine different configurations were investigated under nine different load conditions. Tables 3.7 and 3.8 describe each of the configurations and load cases studied, respectively.

Table 3.7 Joined Wing Model Configurations

Configuration Number	Aft Wing Description
1	No Aft Wing Ribs; No Slit Original Joint Layout
2	No Aft Wing Ribs; Slit Present Original Joint Layout
3	Aft Wing Ribs Present; No Slit Original Joint Layout
4	Aft Wing Ribs Present; Slit Present Original Joint Layout
5	Aft Wing Ribs Present; Slit Present Original Joint Layout; Unconstrained Slit
6	Aft Wing Ribs Present; No Slit New Joint Layout
7	Aft Wing Ribs Present; Slit Present New Joint Layout
8	Aft Wing Ribs Present; Slit Present New Joint; Unconstrained Slit
9	Aft Wing Ribs Present; Slit Present New Joint Layout; New Joint Fixities

Table 3.8 Joined Wing Model Load Cases

Load Case Number	Description
1	2.5g Maneuver Load with Full Fuel Load
2	2.5g Maneuver Load with Zero Fuel Load
3	Turbulent Gust Encounter During Cruise
4	-1.75g Impact with Full Fuel
5	±15° Aft Wing Twist
6	2.5g Maneuver Load with Full Fuel Load and ±15° Aft Wing Twist
7	2.5g Maneuver Load with Zero Fuel Load and ±15° Aft Wing Twist
8	Turbulent Gust Encounter During Cruise and ±15° Aft Wing Twist
9	-1.75g Impact with Full Fuel and ±15° Aft Wing Twist

The loads were developed by Rasmussen and applied to the model as nodal forces [31, 32]. For the new joint design, these loads would be slightly less than for the original joint layout. This was due to the loss of surface area and the reduction in node and element numbers brought about by the redesign.

The boundary conditions used in the analyses did not vary for the forward wing. Both forward wing spars were fully constrained at the root. The aft wing's forward spar remained constrained in all directions but was allowed free rotation about the global *y-axis* for Configurations #1-8. This simulates a typical flying tail or stabilator design, where the entire surface is mounted by a single actuated torque tube as shown in Figure 3.14 [1]. The aft wing's aft spar was fully constrained at the joint for all cases and at the root for

load cases #1-4. For the remaining load cases, a $\pm$0.50 m (1.64 ft) forced displacement was imposed at the spar. This provided approximately 15° of twist to the aft wing.

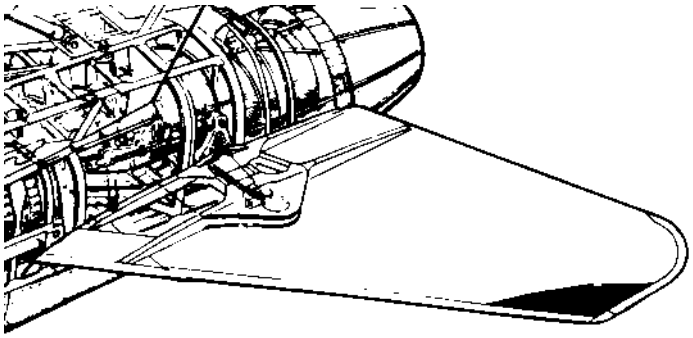

Figure 3.14 Example of a Stabilator

Configurations #1 and #2 were used as initial test cases to determine the effects of adding a slit and altering the composite ply orientations of the CLAS carbon fiber skins, as well as debugging the model. Configurations #3 and #4 were used to validate the findings from #1 and #2 against a more realistic structural model. Configurations #6 and #7 were used to test the performance of the new joint design under the same loading conditions as the original joint layout. Although the loads between the original and new joint designs were not identical, conclusions could still be drawn from comparing them against one another.

Configurations #5 and #8 differ from their counterparts in that there are no constraints imposed on the nodes along the slit. This was done to gain some insight into the behavior of the slit. By seeing visibly the translation of the slit relative to the rest of the structure, some insight into the mechanism for the development of the constraint forces holding the slit together in the other models may be attained.

Configuration #9 is a special case of configurations #6-8. In this model, the fixities of the aft wing's forward and aft spar have been changed. The front spar is constrained against translation in all three directions and unconstrained against any rotation, thus simulating a ball joint. In one case, the aft spar is constrained at the joint by a ball joint and free at the root (allowing the twist moment to be applied). In the other case, the joint end is free in all directions and for all rotations, simulating a fully flying aft wing.

IV. Results and Analysis

4.1 Overview

This chapter describes the results of this research. These results are presented according to several important parameter variations and structural behaviors. Because of the large volume of data collected during this research, a representative sample is provided here. Further results are provided in the appendices for reference.

4.2 Laminate Ply Orientation

The orthotropic nature of composite materials allows them to be manufactured in such a way as to allow the final structural behavior to react in a specific way. This process is known as tailoring and is accomplished by orienting the strong direction of each ply (usually the fiber direction) in certain combinations throughout the laminate construction.

In the previous models of the sensorcraft, a symmetrical lay-up was used to acquire a quasi-isotropic laminate. This research examined what effect changing the ±45° plies of this laminate would have on the amount of twist being induced into the aft wing for a given applied force. To accomplish this, a 1000 N force was applied to the aft wing's aft spar in the positive z-direction, simulating an applied actuator load. This allowed comparisons to be made between models with and without slits at the various orientation angles. Table 4.1 shows the resulting twist angles obtained from the analyses.

Table 4.1 Effects of Aft Wing Skin Ply Orientation Variation

Ply Orientation	Without Slit (deg/1000 N)	With Single Slit (deg/1000 N)	With Two Slits (deg/1000 N)
Original ±45° plies unchanged	0.08829	0.46025	0.47466
±45° plies changed to ±22.5° on Upper skin only	0.09420	0.45728	0.51775
±45° plies changed to ±67.5° on Upper skin only	0.09300	0.46830	0.53442
±45° plies changed to ±22.5° on Both skins	0.10054	0.47092	0.51817
±45° plies changed to ±67.5° on Both skins	0.09720	0.45511	0.53467
+45° plies changed to 0° and -45° plies changed to 90°on Upper skin only	0.10273	0.47058	0.52888
+45° plies changed to 0° and -45° plies changed to 90°on Both skins	0.11515	0.46898	0.52938

For the unmodified wing, the ±45° orientation was found to be the worst case, while the last case was the best, with a 30% improvement. The single slit, located at the lower flange of the aft wing's aft spar, only had a 3% improvement between its best and worst cases; whereas, the two slits, located at the lower flange of the aft wing's aft spar and at the upper flange of the forward spar, had a 12% improvement. Overall, the single slit allowed an average of 373% more twist than the unmodified wing. The two slit configuration allowed an average of 429% more twist.

Most interesting, however, was the tendency of the single slit configuration to favor a smaller ply orientation (closer to 0°); whereas, the two slit configuration favored a larger ply orientation (closer to 90°). The difference between these two configurations

averaged only 12%, with the two slits being better in all cases. This difference, however, is likely not sufficient to warrant the additional structural complexity required by the two slit design.

4.3 Effect of a Spanwise Slit

As already seen in Table 4.1, the addition of a spanwise slit into the wing geometry produces a profound effect on the amount of twist that can be induced into the wing structure. The use of the slit produces one of the effects in the cross-section already mentioned in Chapter III: either an increase in strain, a decrease in applied moment or some combination of the two. This section addresses what those effects would be.

In examining the forces present in a laminated material, stress is usually not as insightful of a measure as in a typical isotropic material. This is due to both the thickness and orientation variations within each ply of the laminate, which are not present in an isotropic material. Thus, for a given applied load, the stress will vary in magnitude and direction for each ply of the laminate. If, however, the laminate is relatively thin, it can be assumed that the strain will remain constant throughout the laminate thickness, since it all must deform together. This makes strain a better indicator of the forces within a laminate; therefore, it will be used in the comparisons presented below.

For a forced deflection of 0.5 m of the aft wing's aft spar, corresponding to approximately 15° of twist, the configurations without the spanwise slit (please refer to Table 3.7 for the configuration definitions) created over two times the amount of internal strain compared to the untwisted load cases. Adding the slit did not affect the strain for

the untwisted wing very much, in most cases it stayed about the same magnitude. Once the wing was twisted, however, the strains were about 50% less than that of the wing without the slit in all load cases. Table 4.2 shows the results for configurations #1-4 for load case #5, aft wing twist only, and Table 4.3 shows the results for load cases #2 and #7, the +2.5g maneuver without fuel cases with and without twist, respectively.

Table 4.2 Aft Wing Strains Due to Twist Only

Configuration		von Mises Strain	
		+15° Twist	-15° Twist
1 No slit; No ribs	Linear	$5.12 \cdot 10^{-3}$	$5.12 \cdot 10^{-3}$
	Nonlinear	$5.52 \cdot 10^{-3}$	$4.84 \cdot 10^{-3}$
2 Slit; No ribs	Linear	$3.09 \cdot 10^{-3}$	$3.09 \cdot 10^{-3}$
	Nonlinear	$3.18 \cdot 10^{-3}$	$3.09 \cdot 10^{-3}$
3 No slit; Ribs	Linear	$6.23 \cdot 10^{-3}$	$6.23 \cdot 10^{-3}$
	Nonlinear	$5.94 \cdot 10^{-3}$	$5.15 \cdot 10^{-3}$
4 Slit; Ribs	Linear	$4.29 \cdot 10^{-3}$	$4.29 \cdot 10^{-3}$
	Nonlinear	$4.15 \cdot 10^{-3}$	$3.58 \cdot 10^{-3}$

Table 4.3 Aft Wing Strains Due to Twist and Aerodynamic Loads

Configuration		von Mises Strain		Percent Difference
		Load Case 2	Load Case 7	
1 No slit; No ribs	Linear	$2.44 \cdot 10^{-3}$	$5.22 \cdot 10^{-3}$	113.9
	Nonlinear	$2.51 \cdot 10^{-3}$	$5.21 \cdot 10^{-3}$	107.6
2 Slit; No ribs	Linear	$2.53 \cdot 10^{-3}$	$3.64 \cdot 10^{-3}$	43.9
	Nonlinear	$2.47 \cdot 10^{-3}$	$3.39 \cdot 10^{-3}$	37.2

Table 4.3 (Continued) Aft Wing Strains Due to Twist and Aerodynamic Loads

Configuration		von Mises Strain		Percent Difference
		Load Case 2	Load Case 7	
3 No slit; Ribs	Linear	$2.50 \cdot 10^{-3}$	$6.14 \cdot 10^{-3}$	145.6
	Nonlinear	$2.49 \cdot 10^{-3}$	$5.59 \cdot 10^{-3}$	124.5
4 Slit; Ribs	Linear	$2.69 \cdot 10^{-3}$	$4.76 \cdot 10^{-3}$	77.0
	Nonlinear	$2.46 \cdot 10^{-3}$	$4.01 \cdot 10^{-3}$	63.0

Figures 4.1 and 4.2 below shows the nonlinear strain contours for load case #5, while Figures 4.3 and 4.4 below show the nonlinear strain contours for load case #7 for configurations #3 and #4, respectively. These help to illustrate the results presented in Tables 4.2 and 4.3 above.

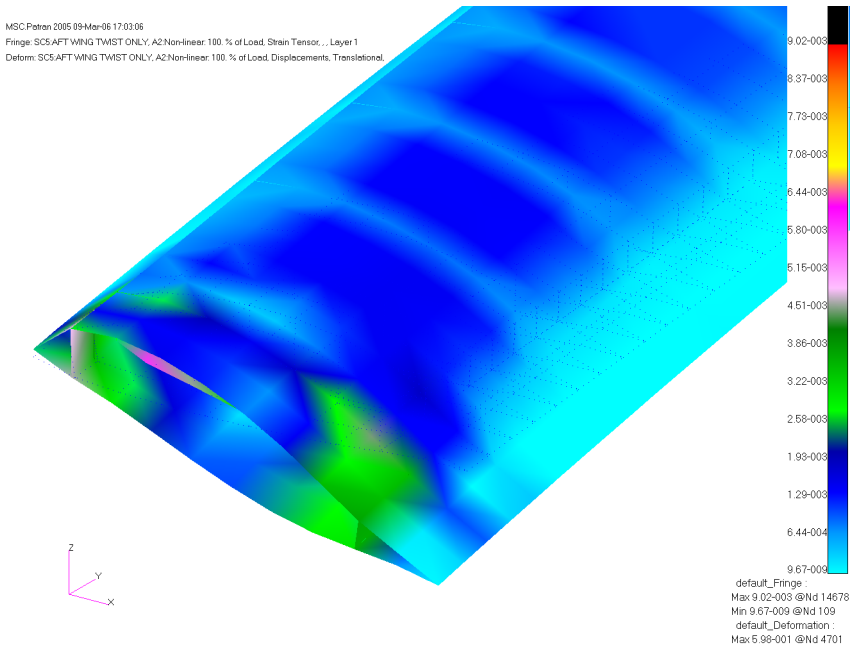

Figure 4.1 Nonlinear Strain Contour for Configuration #3, Load Case #5

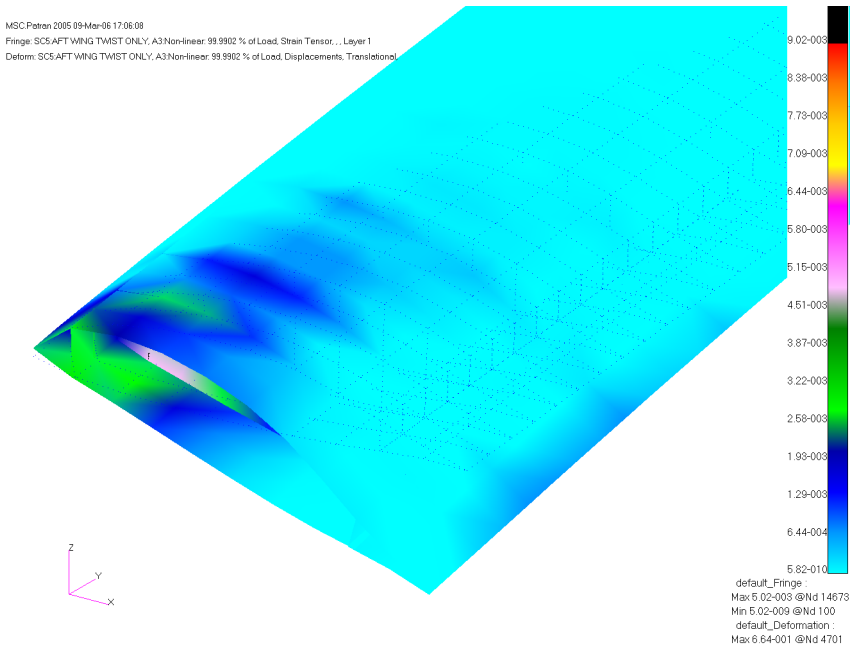

Figure 4.2 Nonlinear Strain Contour for Configuration #4, Load Case #5

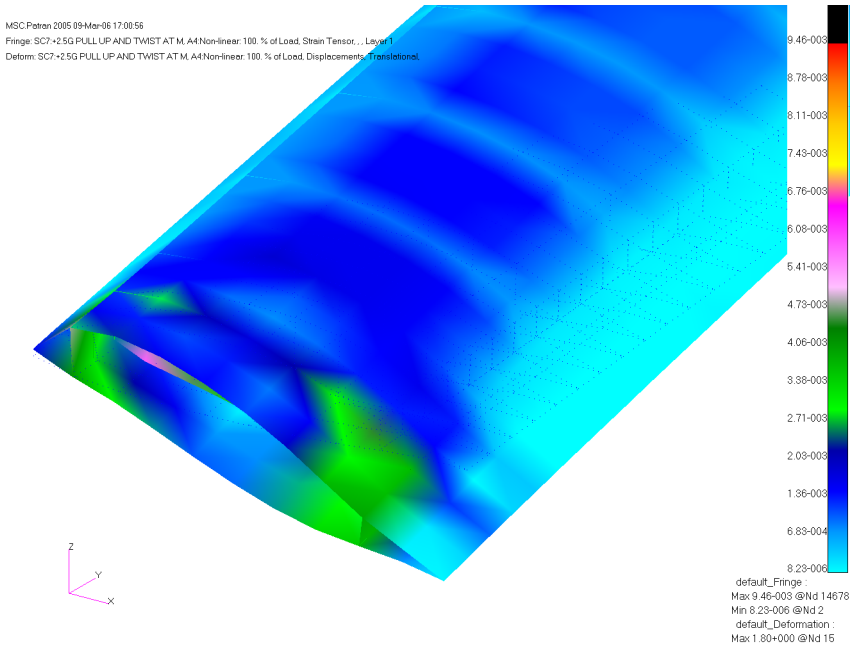

Figure 4.3 Nonlinear Strain Contour for Configuration #3, Load Case #7

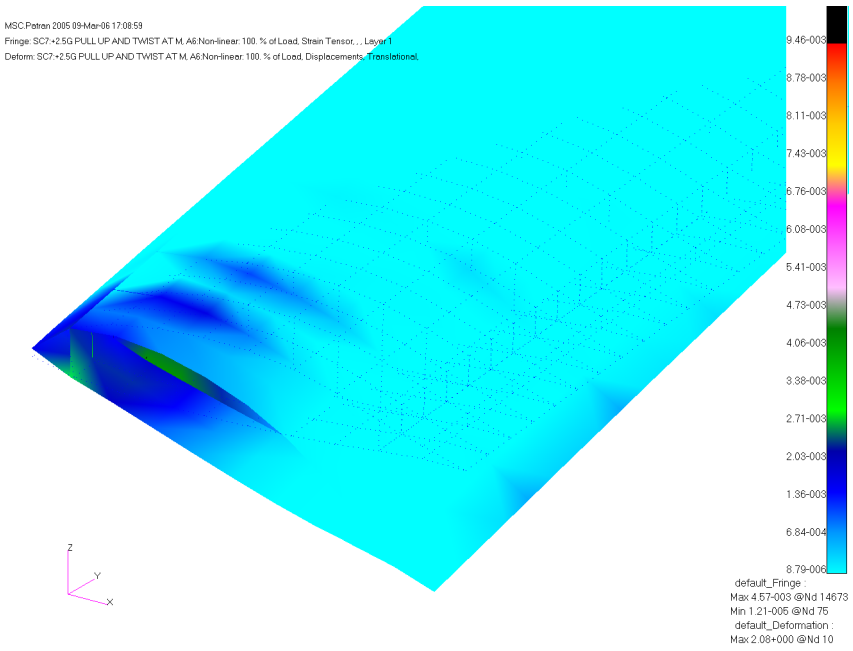

Figure 4.4 Nonlinear Strain Contour for Configuration #4, Load Case #7

The effect of the lower moment magnitude appears globally in the wing as well. Figure 4.5 shows clearly that the strain is much higher in the configuration #3 without the slit and continues at a relatively constant magnitude for the entire span of the aft wing. Configuration #4, that has a slit, not only has a smaller magnitude of strain in the upper skin, but the strain is very localized to the forward spar of the aft wing, as shown in Figure 4.6. The significant benefit of the slit is easily seen by comparing the two plots.

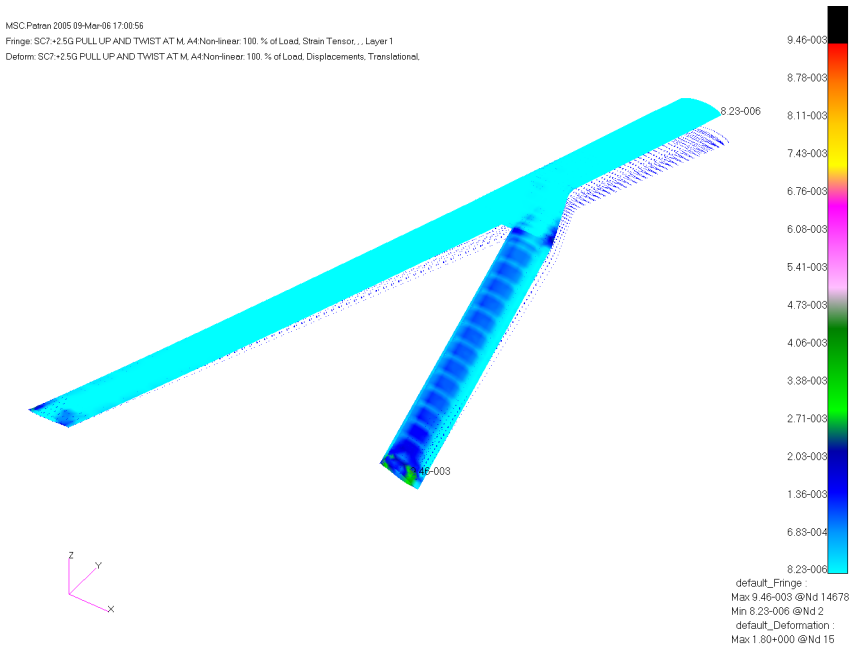

Figure 4.5 Global Nonlinear Strain Contour for Configuration #3, Load Case #7

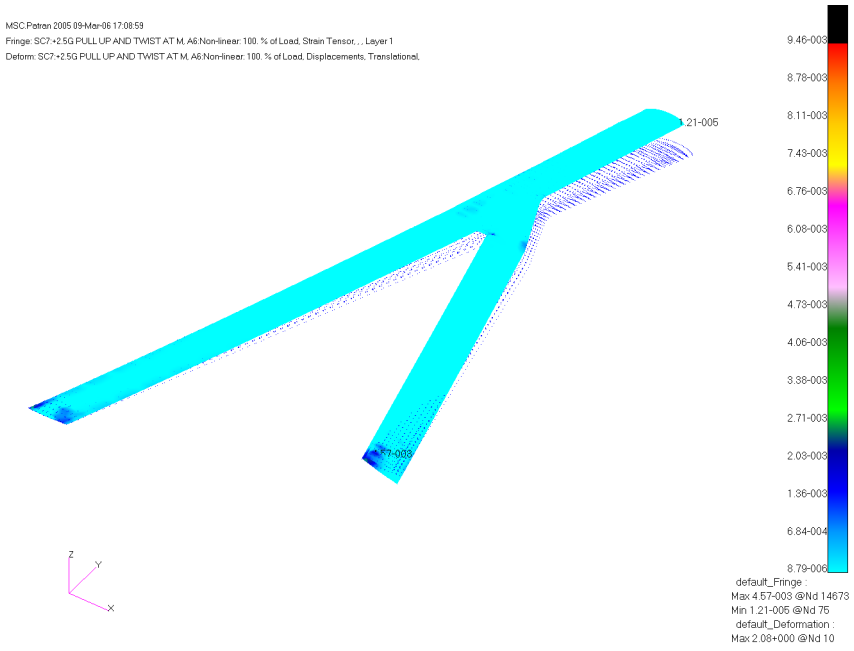

Figure 4.6 Global Nonlinear Strain Contour for Configuration #4, Load Case #7

4.4 Aft Wing Twist Distribution

One important parameter is the distribution of the induced twist along the span of the aft wing. Optimally, the majority of twist should be near the root of the aft wing, where the moment arm from the aircraft's center of gravity is the greatest. Moving along the span of the aft wing toward the joint, the aft wing's moment arm decreases, thereby decreasing the control power created by the twist. Figure 4.7 shows the twist distributions for Configuration #1-4 versus the aft wing span for load case #5, the twist only case.

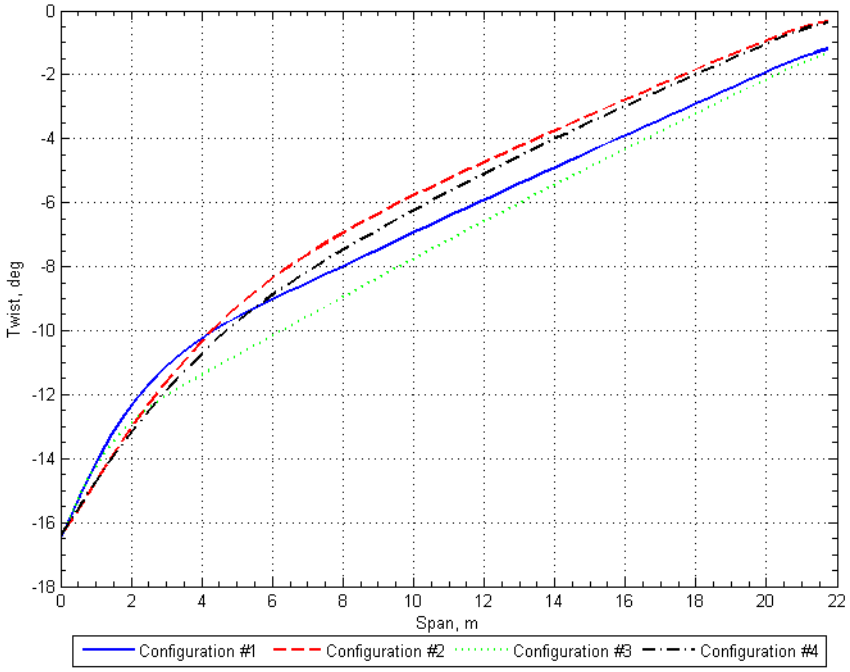

Figure 4.7 Twist Distribution for Configurations #1-4, Load Case #5

Figure 4.8 shows the twist distributions for the same configurations presented above for load case #7, the gust load.

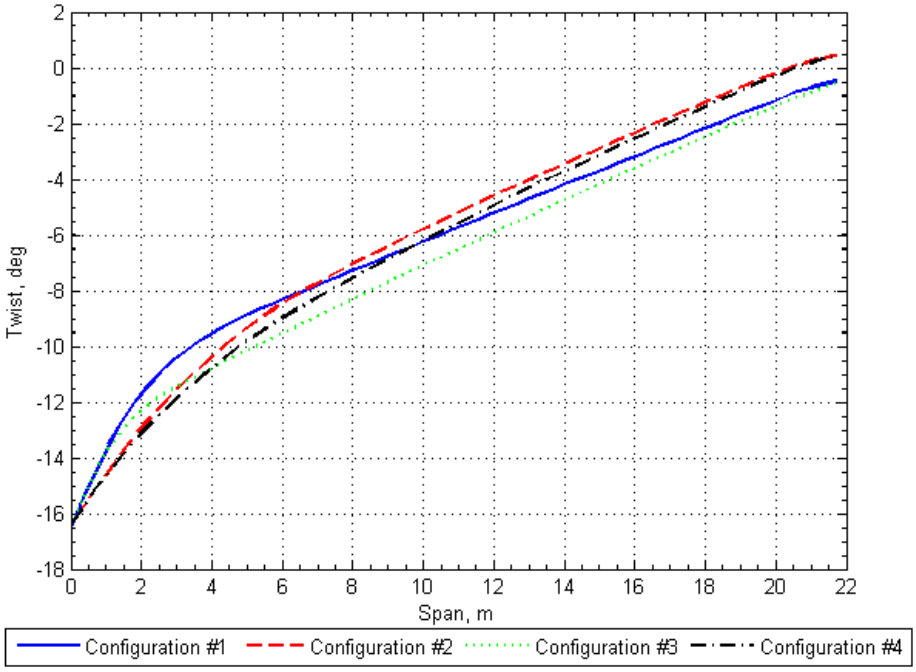

Figure 4.8 Twist Distribution for Configurations #1-4, Load Case #7

These results show a relatively linear twist distribution, especially in the configurations with the slit (#2 and #4). The hook near the root results from the dissipation of strain energy in the region near the applied twist load. The lack of the ribs and the presence of the slit allowed the aft spar to be somewhat free to rotate aft and up or forward and down, depending upon the direction of the load. With this type of behavior, the cross-section has a tendency to warp in the plane of the cross-section, as is clearly shown in Figure 4.9. It is also worth noting that these results provide an excellent example of St. Venant's Principle that a concentrated load's effects on the stress/strain in the structure are only substantially different near the region of application of the force.

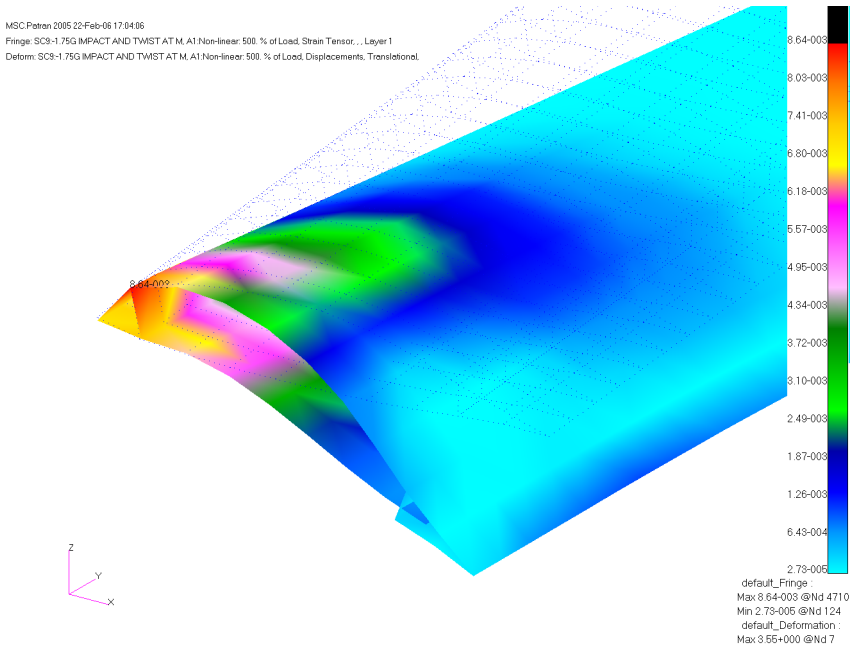

Figure 4.9 Nonlinear Strain Contour for Configuration #2, Load Case #9

4.5 Slit Behavior and Restraint Forces

The structural design of the slit mechanism relies on two important parameters: the translation of the slit in the relative xy-plane of the aft wing and the magnitude of the forces required to restrain the lower skin from movement in the relative z-direction. The displacement of the lower skin, primarily in the chordwise direction, determines the length of the aft spar's lower flange and the size of the stop block required. The magnitude of the forces required to keep the slit from pulling apart also determines the material thicknesses of the flange and stop block.

Figure 4.10 below shows the displacements of the slit in the chordwise direction for configuration #2 (having no aft wing ribs) and configuration #4 (having aft wing ribs).

Positive values indicate the slit is trying to close up, and negative values indicate the slit is trying to spread apart. By comparing the two, the benefit of incorporating the ribs is very apparent. Without the ribs, the slit exhibits excessive movement, requiring the stop block and spar flange to be very large. The ribs alleviate these large displacements, making the size of the flange and stop block much more manageable. Unfortunately, this alleviation tends to increase the strain being carried by the ribs, especially in the region near the aft wing root, as is shown in Figure 4.11.

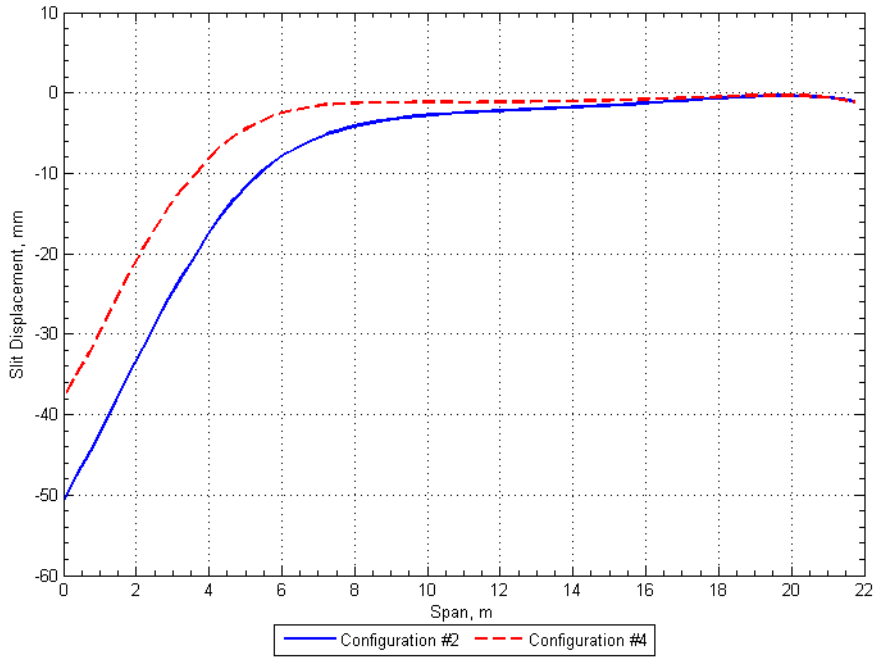

Figure 4.10 Chordwise Slit Displacement for Configurations #2 and #4, Load Case #7

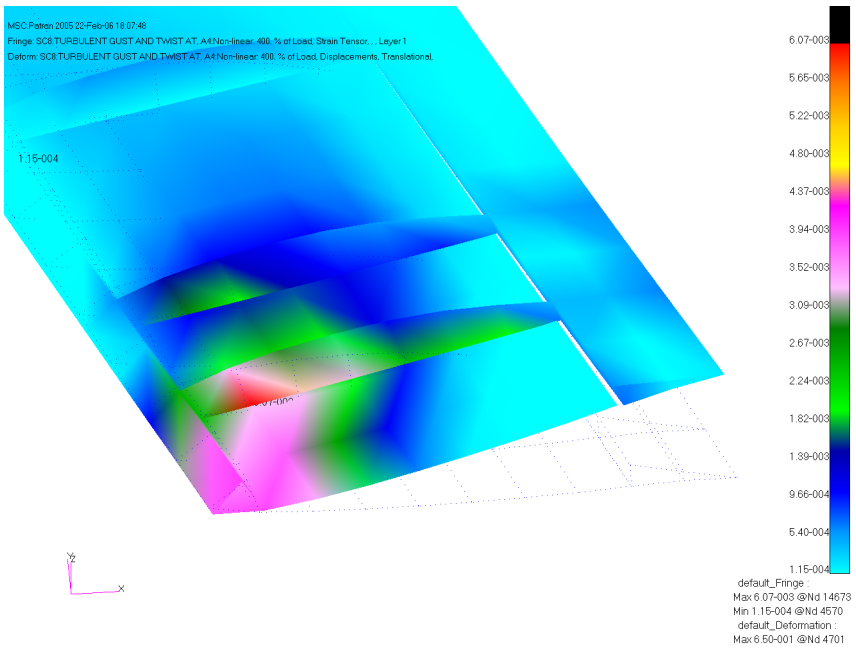

Figure 4.11 Nonlinear Strain Contour for Configuration #7, Load Case #8

The relative magnitudes of the forces required to restrain the slit against coming apart in the vertical direction is presented in the following figures. The following figures show the forces necessary to restrain configurations #2 and #4 for load case #5 (twist only) for a +15° twist (Figure 4.12) and a -15° twist (Figure 4.13). These forces restrain the slit from pulling apart vertically.

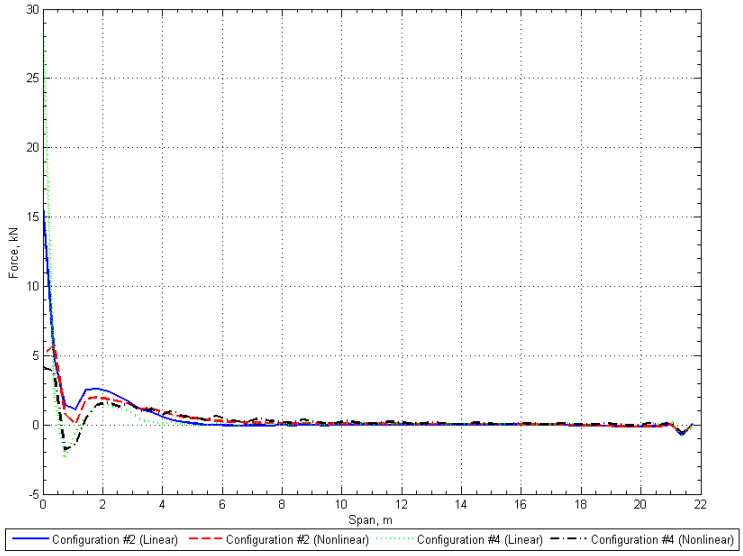

Figure 4.12 Slit Vertical Restraint Forces for Configurations #2 and #4 under a +15° Twist Load Only

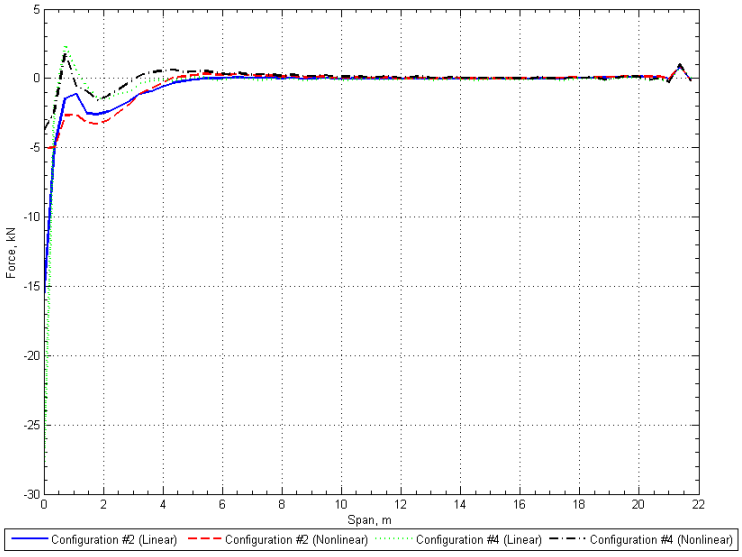

Figure 4.13 Slit Vertical Restraint Forces for Configurations #2 and #4 under a -15° Twist Load Only

Most notable of these results is the overall low magnitudes of the restraint forces. Outboard of about four meters in span, the forces are less than 1000 N. Only within these first few meters do the forces grow to around 5000 N. This is primarily due to the strain energy being able to be dissipate through more material, due to the presence of the ribs in configuration #4.

Also notable in these plots is the sharp divergence between the linear and nonlinear results. This is attributed to the large amount of twist being induced into the wing at the aft spar root. Although the force is only around 5000 N, the large amount of twist being sought violates the assumptions of small displacements and small rotations that are made in a linear, Euler-Bernoulli beam analysis. This violation results in the calculated forces being much higher than are actually required.

How the forces change under aerodynamic loads with and without twist was also considered. Figure 4.14 shows configuration #4 undergoing enforced twist angles of -15°, 0° and +15° during a +2.5g maneuver without fuel. Fortunately, as will be seen in the figures below, the restraint forces do not increase significantly.

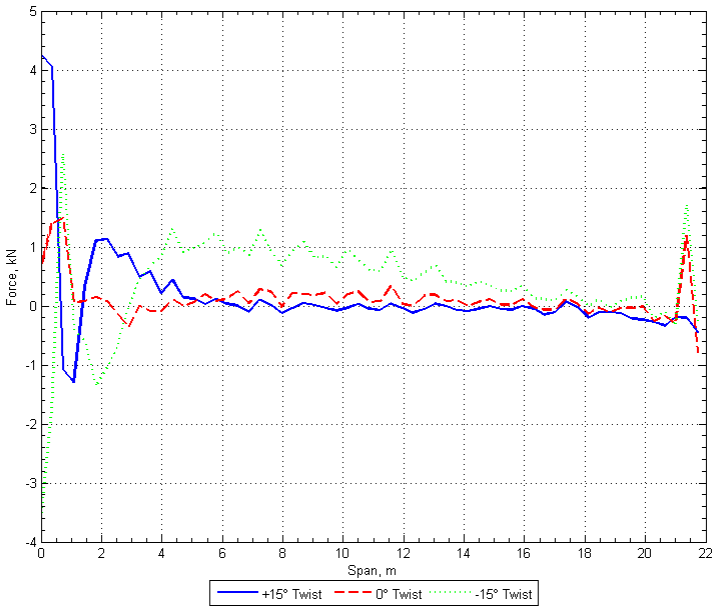

Figure 4.14 Slit Vertical Restraint Forces for Configuration #4 with Twist and Aerodynamic Loads

To further investigate the effects of the restraint forces, another configuration (#5) was examined which eliminated the vertical constraints on the slit. As a comparison, the strain contours for configurations #4 and #5 are shown in Figures 4.15 and 4.16 below. As can clearly be seen, although the actual restraint forces are relatively small, the absence of them produces some very deleterious effects in both the displacement of the lower skin and the strain in the upper skin and ribs. These effects are due primarily to the decrease in the load being carried by the lower skin and must then be picked up by the remaining structural elements.

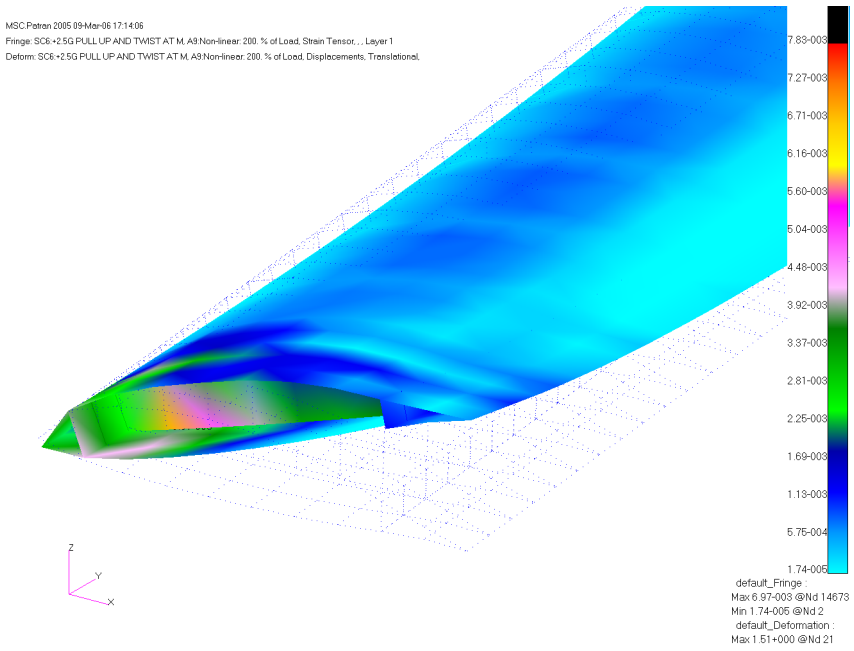

Figure 4.15 Nonlinear Strain Contour for Configuration #4, Load Case #6

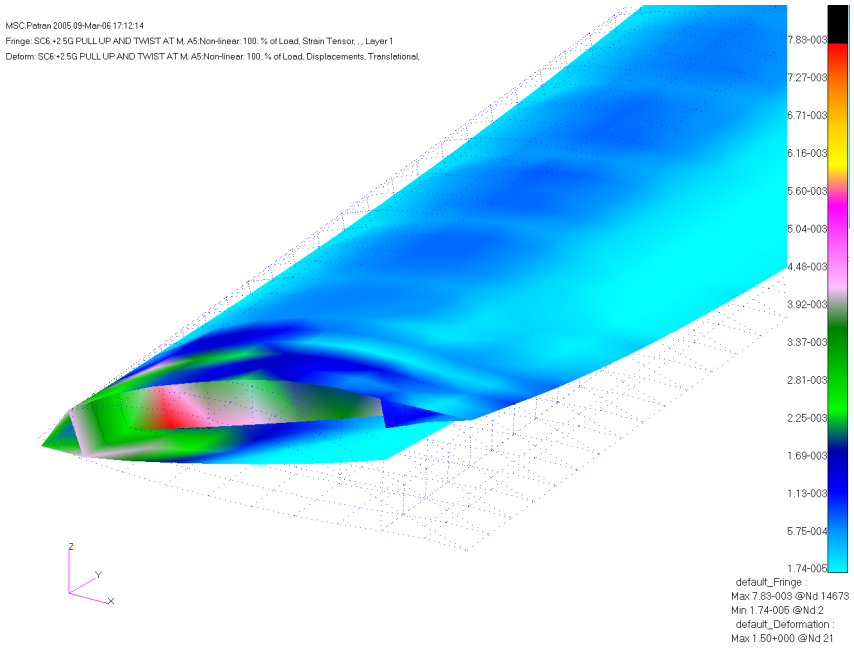

Figure 4.16 Nonlinear Strain Contour for Configuration #5, Load Case #6

4.6 Buckling Results

Buckling has been shown, by several previous authors, to be a critical factor in the joined wing design. Indeed, no analysis of a joined wing would truly be complete without some consideration of buckling. To this end, Table 4.4 presents the results of the buckling analyses conducted in this study for load cases #1-4.

Table 4.4 Buckling Eigenvalues for Original Joint Design

Configuration	Buckling Eigenvalue			
	Load Case 1	**Load Case 2**	**Load Case 3**	**Load Case 4**
1 No Slit; No Ribs	4.9777	4.4676	6.6919	3.8367
2 Slit; No Ribs	3.3623	3.0137	4.5346	0.8945
3 No Slit; Ribs	5.3368	4.8367	7.3001	3.8762
4 Slit; Ribs	4.0902	3.6663	5.5072	1.0418

As indicated in Table 4.4 above, the impact load case for configuration #2 has already begun to cause buckling, as is shown in Figure 4.17 below. Since this is one of the configurations with a slit, the buckling eigenvalue has already been reduced from what it would have been had no slit been present (as in configuration #1). This reduction was already expected, but the severity of the impact load case serves to highlight the issue.

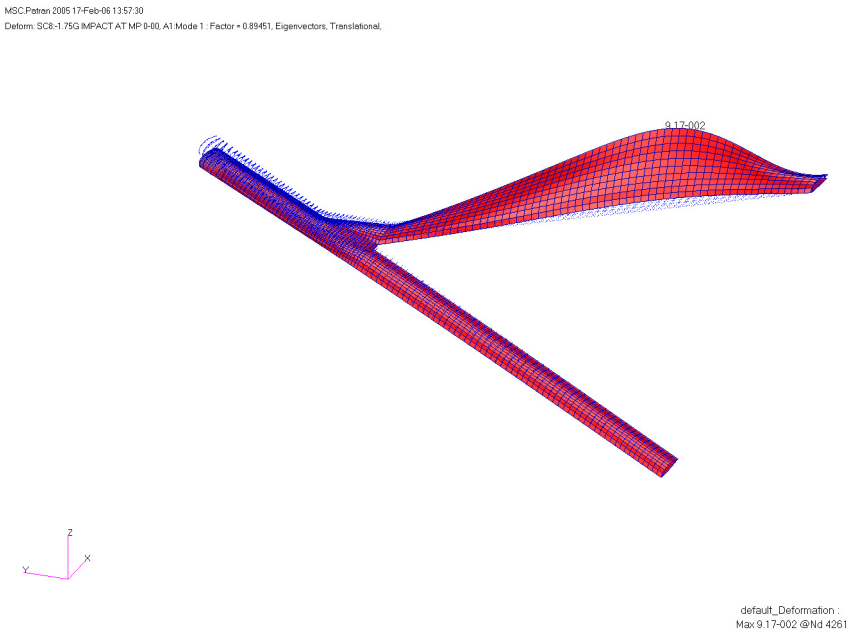

Figure 4.17 Buckling Mode Shape for Configuration #2, Load Case #4

Figure 4.18 below shows the typical buckling mode shape for the maneuver and gust load cases, while Figure 4.19 shows the typical mode shape for the impact load cases. A word of caution must be mentioned at this point about buckling eigenvalues and mode shapes, particularly for the gust load cases. Buckling eigenvalues represent a scale factor, that when applied to the reference load, would give the actual load required to cause buckling in a structure. The sign of the eigenvalue represents whether the reference load would need to be applied in a certain direction. This directly relates to the shape of the buckling mode. If the eigenvalue is positive and is applied to the reference load, the structure will buckle in one direction. If, however, the eigenvalue is negative and is applied to the reference load, the structure will buckle in the opposite direction. Thus, the mode shapes below for the gust loads would actually be in the opposite direction than that indicated in the figure.

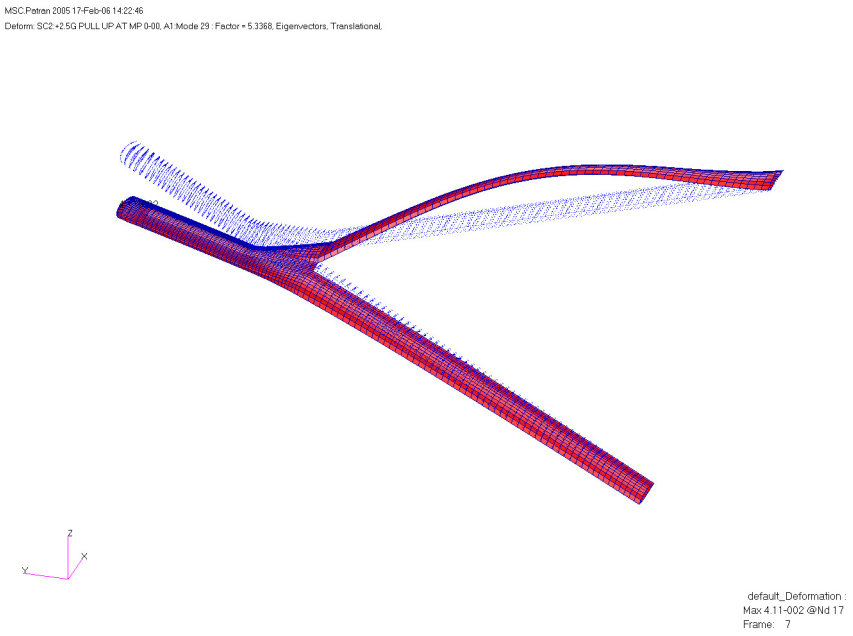

Figure 4.18 Buckling Mode Shape for Configuration #3, Load Case #1

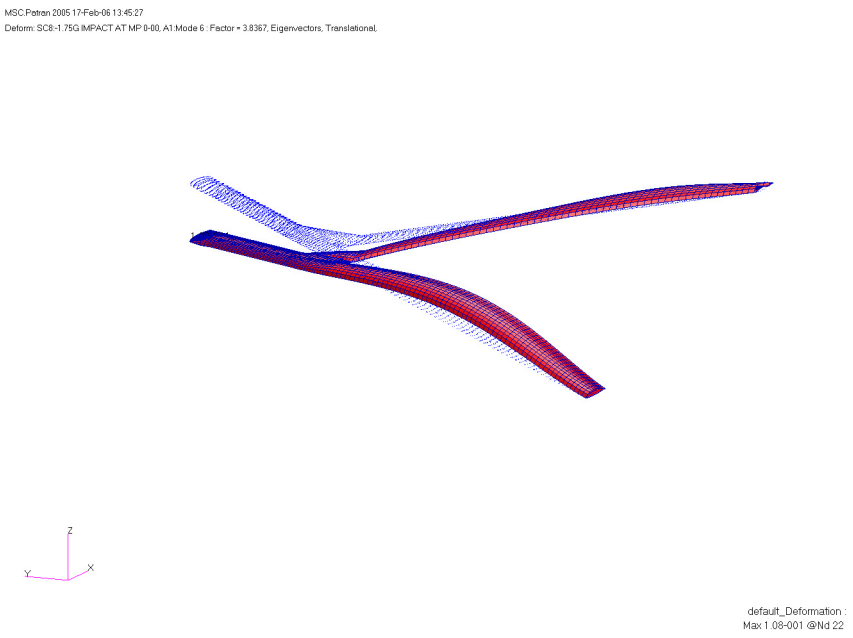

Figure 4.19 Buckling Mode Shape for Configuration #1, Load Case #4

4.7 New Joint Section Design

The analysis of the new joint design examined the same basic parameters studied for the original joint design. Three configurations were analyzed: one with no slit (#6), one with a slit (#7), and one with the unrestrained slit (#8). Unfortunately, due to the approximations used in assigning the loads and element thicknesses over the new joint section, no absolute, direct comparison between the two joint designs can realistically be made. The one load case that does allow some meaningful comparison between the two is the twist only load case (#5).

The strains between the two joint designs under this load case are nearly the same, being within 15% of one another. Neither design seems to have a major advantage over the other. The buckling analysis of the new design did produce eigenvalues that were about 25% higher than the original design. These eigenvalues are presented in Table 4.5.

Table 4.5 Buckling Eigenvalues for the New Joint Design

Configuration	Buckling Eigenvalue			
	Load Case 1	**Load Case 2**	**Load Case 3**	**Load Case 4**
6 No Slit	7.2204	5.7687	9.7716	4.0757
7 Slit	5.7523	4.5483	7.6686	1.1558
8 Unconstrained Slit	5.4350	4.4454	7.0123	1.1417

Another interesting result of the buckling analysis developed from the examination of the buckling modes. The original joint had typical buckling modes that were clearly global modes. The new design, however, tended to have buckling modes that included

local crippling of the outboard wing section at the joint, as is shown in Figure 4.20. This indicates a sensitivity to this type of failure in the new design. Since several ribs are already present in the new joint section, the solution probably resides in increasing the skin thicknesses in that area. Accounting for the offset between the major plies of the skins due to the core material would also help alleviate this problem. Figures 4.21 and 4.22 show typical global buckling modes for maneuver/gust loads and impact loads, respectively.

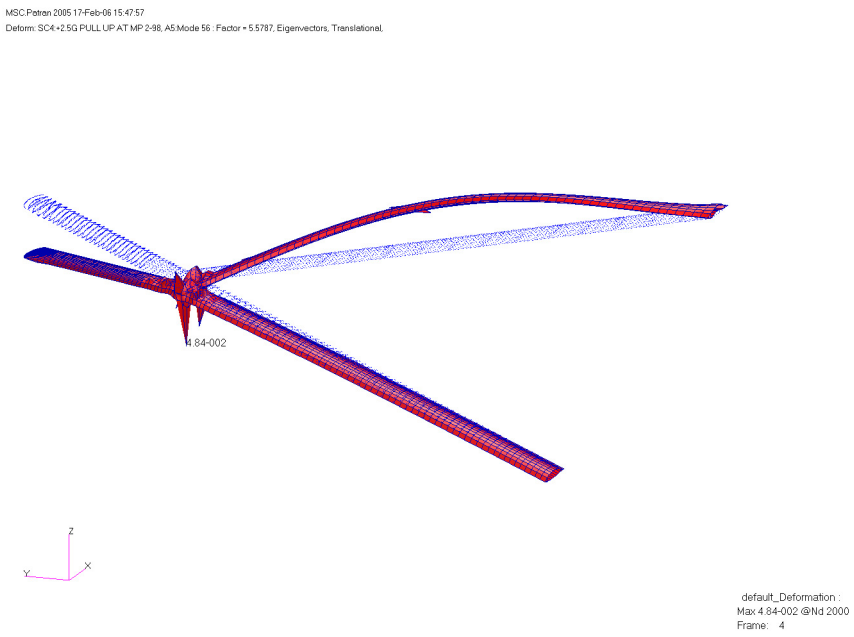

Figure 4.20 Buckling Mode for Configuration #6, Load Case #2

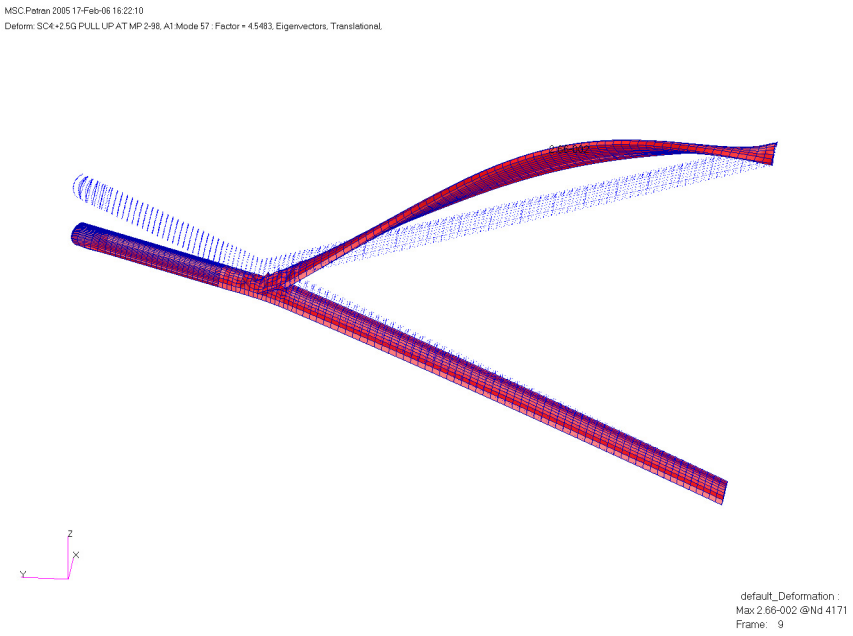

Figure 4.21 Buckling Mode for Configuration #7, Load Case #2

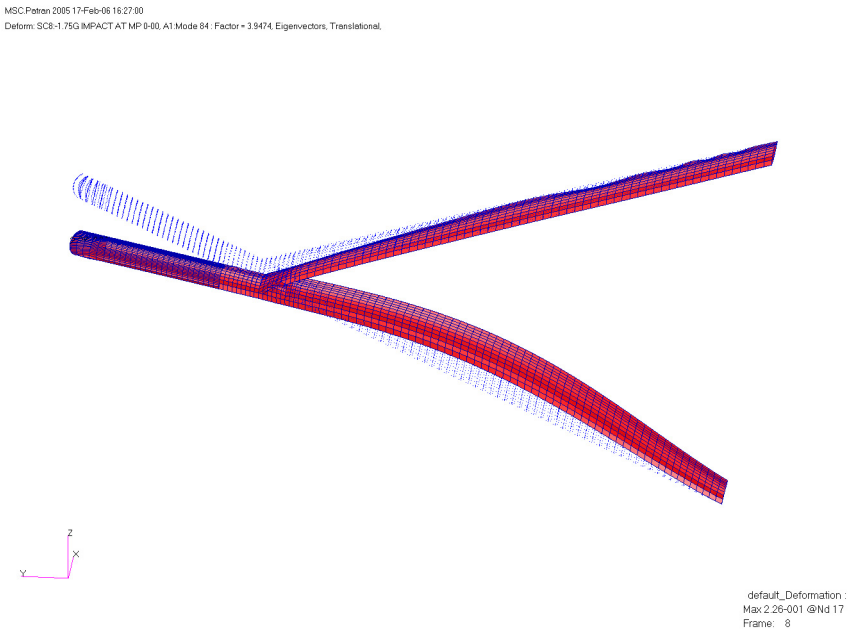

Figure 4.22 Buckling Mode for Configuration #7, Load Case #4

As a final note, it is worth mentioning that this new joint design has not been optimized, as was the original joint design. Indications from the collected data are that this new design has some potential for improvement over the original design, especially considering the similarity in the strain contours between the two designs.

4.8 Aft Wing End Fixity

Several authors have already demonstrated the potential of various end fixities on joined wings [17, 27]. Thus, a couple of different end fixities were investigated for the aft wing spars. The normal configurations had the aft wing's forward spar constrained to allow only rotation about the y-axis. The aft spar root had various constraints depending upon whether twist was being induced into the wing or not. At the joint, both spars were rigidly attached to the joint section. Configuration #9 changed the spar constraints to ball joints (free rotation about all axes) at the joint and forward spar root. Configuration #10 eliminated the aft spar constraint at the joint completely, creating a flying aft wing panel. Both of these configurations were applied to the new joint design.

The result in both configurations was the large reduction of the strains in the aft wing. The resulting strains were on the same magnitude as that of the aerodynamic loads, averaging only about 25-40% higher. Unfortunately, the buckling eigenvalues were also significantly lower as well, being between 25-50% less than that of configuration #7. This difference closely matches the difference in end fixity coefficient between a simple column with one end fixed and one end pinned and another column with both ends pinned.

The fixity coefficients for these two types of columns are: 0.70 and 1.0, respectively, a difference of 30% [25:122].

Figure 4.23 shows the nonlinear strain contour from the maneuver load case (#7) for configuration #9, while Figures 4.24 and 4.25 are the same contours for configuration #10 and #7, respectively. Table 4.6 presents the buckling eigenvalues for configurations #9 and #10.

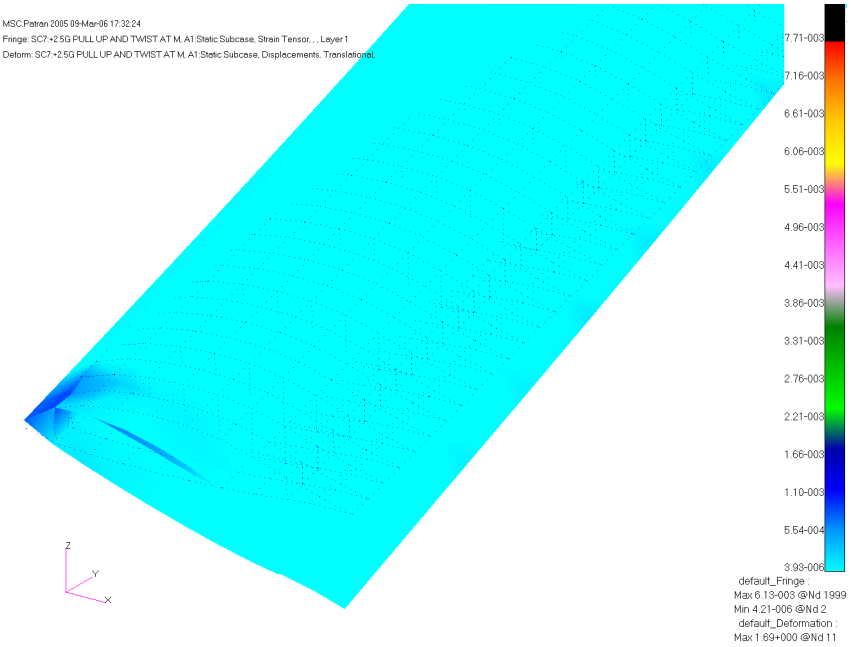

Figure 4.23 Nonlinear Strain Contour for Configuration #9, Load Case #7

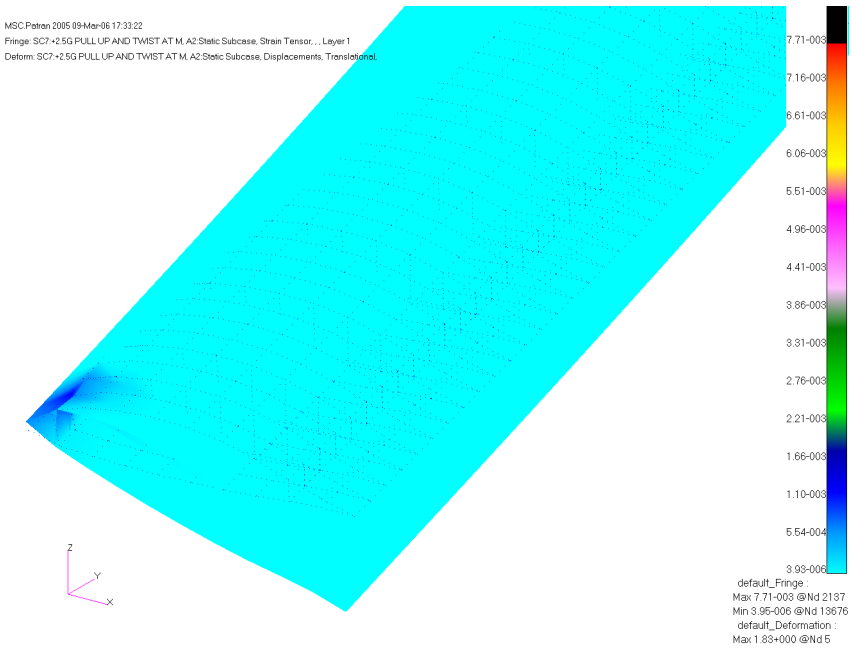

Figure 4.24 Nonlinear Strain Contour for Configuration #10, Load Case #7

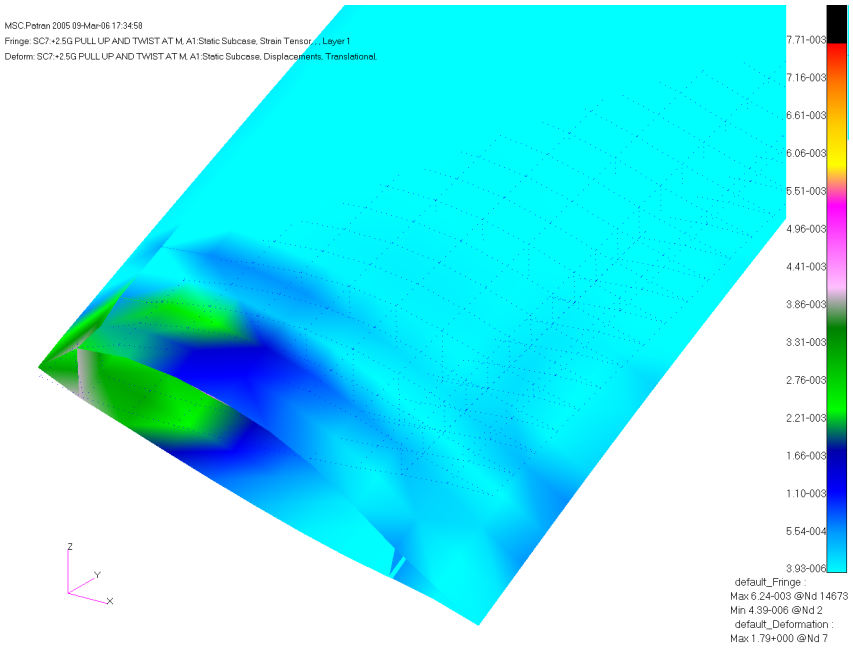

Figure 4.25 Nonlinear Strain Contour for Configuration #7, Load Case #7

Table 4.6 Buckling Eigenvalues for New Joint End Fixities

Configuration	Buckling Eigenvalue			
	Load Case 1	Load Case 2	Load Case 3	Load Case 4
9	4.0109	2.9527	4.8815	1.2048
10	5.4806	3.7061	6.2469	3.7512

It can be seen from Table 4.6 that the new joint design already exceeds the limit loads. Unfortunately, it does not meet the standard factor safety of 1.50. Any structural optimization conducted should take this into account.

Once all of the data is compiled and studied together, a very interesting picture begins to develop. Twisting the aft wing in one direction tended to increase the maximum strains being developed; whereas, twisting the wing in the other direction caused the strains to decrease. This effect can be seen in all of the load cases and throughout all of the configurations. As originally shown by Wolkovtich, the bending plane of a joined wing is inclined. For a high offset between the forward and aft wings, the forward and aft spars can be under different load directions, i.e. one in tension and the other in compression. This is the reason behind the change in strain due to the twist direction.

This fact also helps to explain some of the buckling results as well, such as was shown for configuration #2 in Figure 4.17 above. In this case, a large degree of twist is present in the aft wing. The twist comes from the aft wing's aft spar undergoing a very large compressive load, causing it to buckle, while the forward spar is actually in tension and does not buckle. This proves once again the unique structural qualities inherent in the joined wing concept.

4.9 Actuator Loads

A key factor in the utility of any control design is the amount of force necessary to actuate the control mechanism. By enforcing a specified displacement for the aft wing's aft spar, the forces on the aft spar could then be compared between the different configurations examined. Figure 4.26 shows these results.

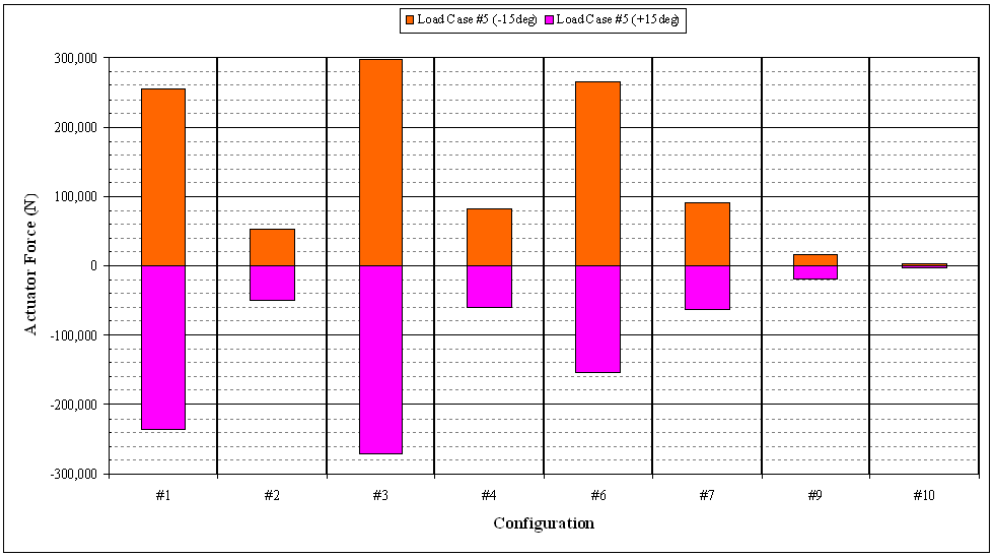

Figure 4.26 Forces Necessary to Induce an Aft Wing Twist of 15°

As is readily apparent, the presence of the slit significantly reduces the forces required to twist the aft wing. Similar to the strain results presented earlier, the slight increases in the required forces can been seen between configurations #2, #4 and #7. Configurations #9 and #10, with the different end fixities on the new joint design, require significantly less force than do the previous configurations. Configuration #10 only required 2400 N (540 lbs) of force. In order to place these values in perspective, the

Boeing F-15E stabilator actuator produces approximately 125,000 N (28,000 lbs) of force [21].

4.10 Impact Load Case

The impact load case selected for this analysis represented a -1.75g impact while carrying a full fuel load. As evidenced by the data developed during this investigation, this represents a worst case scenario. All indicators presented this case as having the worst performance in almost every category of every configuration. The most notable exception was for a negative twist. This particular case tended to be within the bounds of the other cases. The positive twist case was significantly worse, however.

As such, two options are presented to the designer in this situation. This can be used as a critical design load case, and the aircraft designed to accommodate these loads. Undoubtedly, this would lead to a significantly heavier aircraft in the end. The other and more reasonable option would be to incorporate a fuel venting system into the fuel management system of the aircraft. This is a fairly common industry practice, since many large transport aircraft have maximum take-off weights in excess of their maximum allowable landing weights.

4.11 Effect of Aft Wing Twist Axis Error

Late into the analysis, a significant error was discovered in the definition of the axis about which the aft wing was being twisted. Instead of being twisted about axis of the forward spar, the wing was actually being rotated about the global y-axis (horizontally

outboard). This induced noticeable bowing in the forward spar, as shown in Figure 4.27. Obviously, this causes the strain around the root of the forward spar to be significantly higher than what it should be.

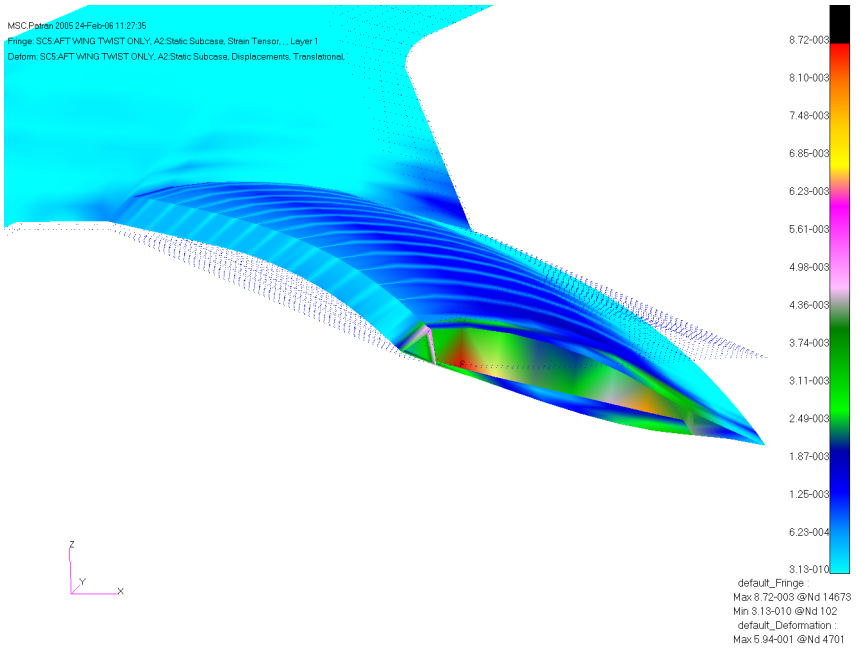

Figure 4.27 Bowing in the Forward Spar of the Aft Wing

In order to quantify the impact of this error, additional linear analyses were conducted using the same load cases and configurations as have already been presented. The results were then compared against the previous data. Figure 4.28 below shows the original, uncorrected strain contour for configuration #4 under the twist load only (load case #5); whereas, Figure 4.29 shows the same configuration and load condition for the corrected case.

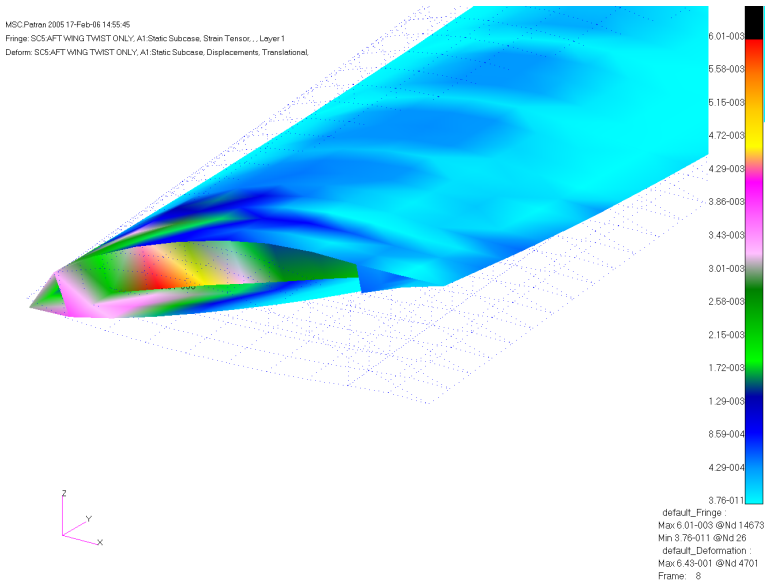

Figure 4.28 Uncorrected Linear Strain Contour for Configuration #4, Load Case #5

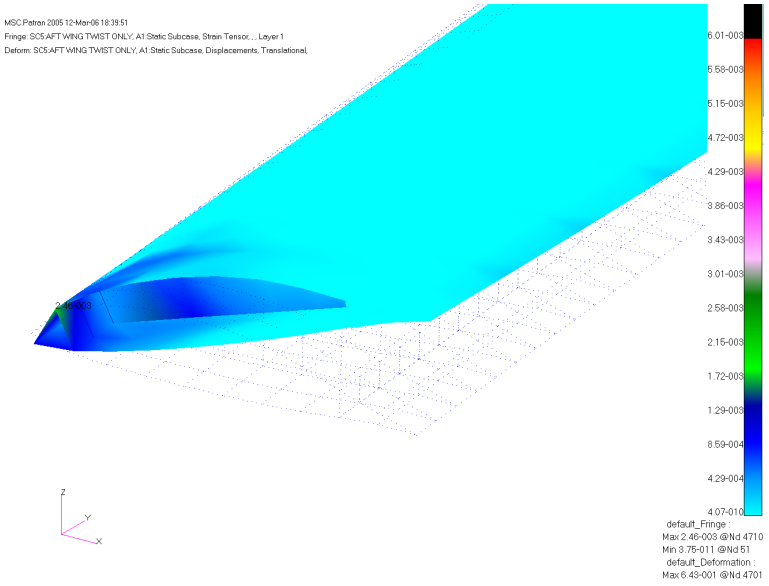

Figure 4.29 CorrectedLinear Strain Contour for Configuration #4, Load Case #5

Similarly, Figures 4.30 and 4.31 below show the same loading conditions for configuration #7 for the uncorrected and corrected cases, respectively.

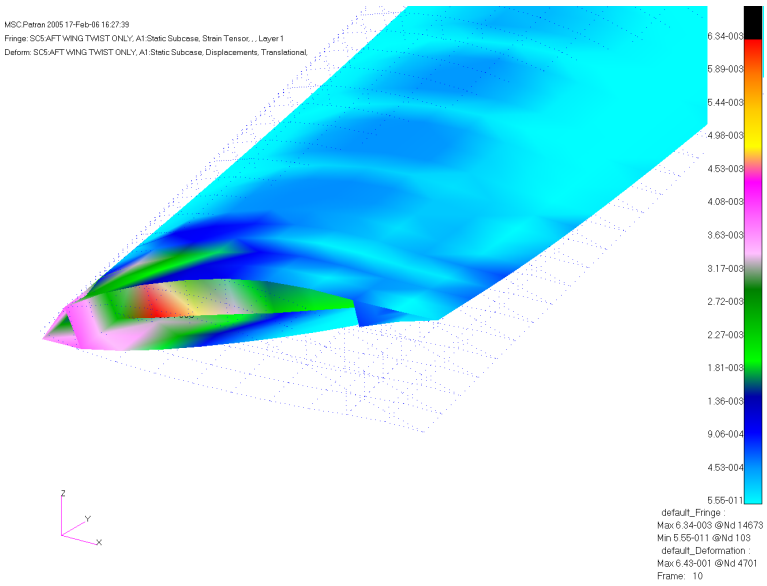

Figure 4.30 Uncorrected Linear Strain Contour of Configuration #7, Load Case #5

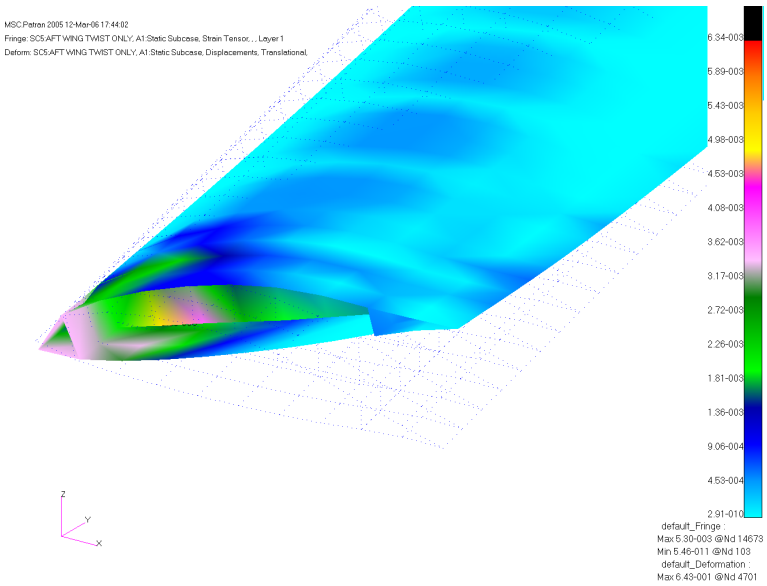

Figure 4.31 Corrected Linear Strain Contour for Configuration #7, Load Case #5

Configuration #4, with the original joint design and slit, has nearly 50% lower strain magnitudes with the corrected axis, dropping from 4.29e-3 to 2.46e-3. Configuration #7 also experiences lower strain magnitudes; however, the difference is not nearly as great as that of configuration #4, as it only dropped from 4.53e-3 to 3.62e-3. This indicates the stiffness of the new joint design is much greater than that of the original, lessening the effect of the axis correction.

Along with the reduction in strain, further reductions in the actuator forces were noted by the correction as well. These force magnitudes tended to be not very significant, as shown in Figure 4.32 below, except in configurations #3 and #4. In configuration #4, the magnitudes dropped by nearly 33% from the original values (around 75,000 N).

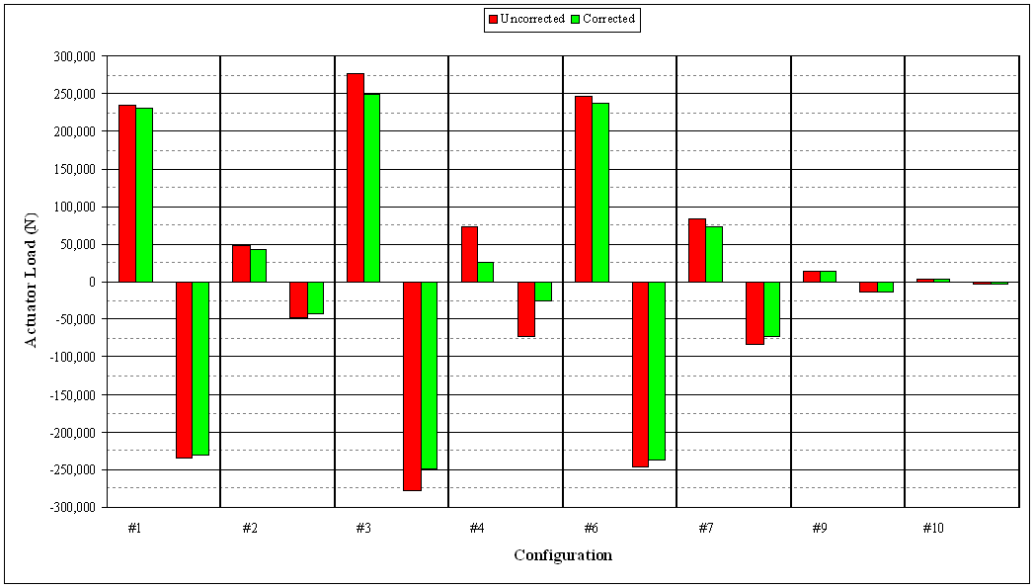

Figure 4.32 Corrected Linear Actuator Forces

In comparisons between the linear and nonlinear analyses results, the actuator forces showed the most variation. The negative twist loading produced very similar magnitudes of both actuator force and strain; however, the positive twist loading condition produced significantly different magnitudes of actuator force (the strain was on the same order as the uncorrected case). The linear analyses conducted in order to determine actuator forces tended to strongly over-predict the required forces in the positive twist cases. This indicates that new nonlinear analyses of configuration #4 would provide much lower forces than is shown in these linear cases.

For configuration #1 and #2, the differences in the results for both strain and actuator force were not that significant. This is due to the large amount of cross-sectional warping at the root already present in these configurations, since no wing ribs are in the

structure. Also, configurations #9 and #10 did not change any since the end fixity boundary conditions were already independent of a specific axis of rotation.

4.12 Flutter Analysis

Because this research involved the development of a viable means to effectively reduce the torsional rigidity of the aft wing structure, a flutter analysis was conducted using ZAERO™ [47]. In order to evaluate the worst case scenario, a flight condition had to be chosen that represented the earliest onset of flutter. The mission profile of the SensorCraft was evaluated to determine where the highest dynamic pressure, and hence the lowest flutter speed, was most likely to occur. This resulted in the selection of Mach 0.50 at sea level on a standard day.

Two types of flutter were evaluated: symmetric and anti-symmetric. Symmetric flutter is simply a case where the both wing tips oscillate in the same direction as one another. Anti-symmetric flutter involves the wing tips oscillating in opposite directions, but with the same magnitudes as one another. This is typically the most common mode of flutter.

One common means of determining the flutter speed is to plot velocity versus damping factor, know as a V-G plot, for each mode. Positive damping indicates instability or flutter; therefore, wherever the mode crosses the x-axis (zero damping), that velocity is the flutter speed. Figure 4.33 below shows the symmetrical flutter modes for configurations #3 and #4, while Figure 4.34 shows the velocity versus flutter frequency

for the two primary modes contributing to the flutter. Figures 4.35 and 4.36 repeat these same plots for the anti-symmetrical flutter case.

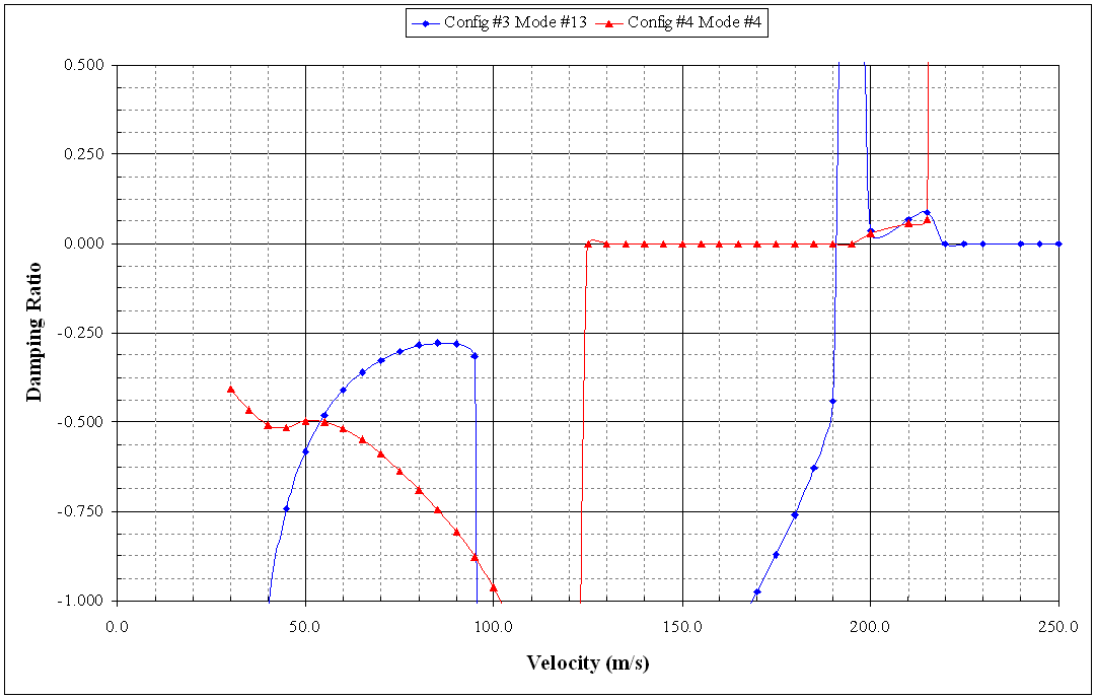

Figure 4.33 Symmterical Flutter Velocity versus Modal Damping Ratio

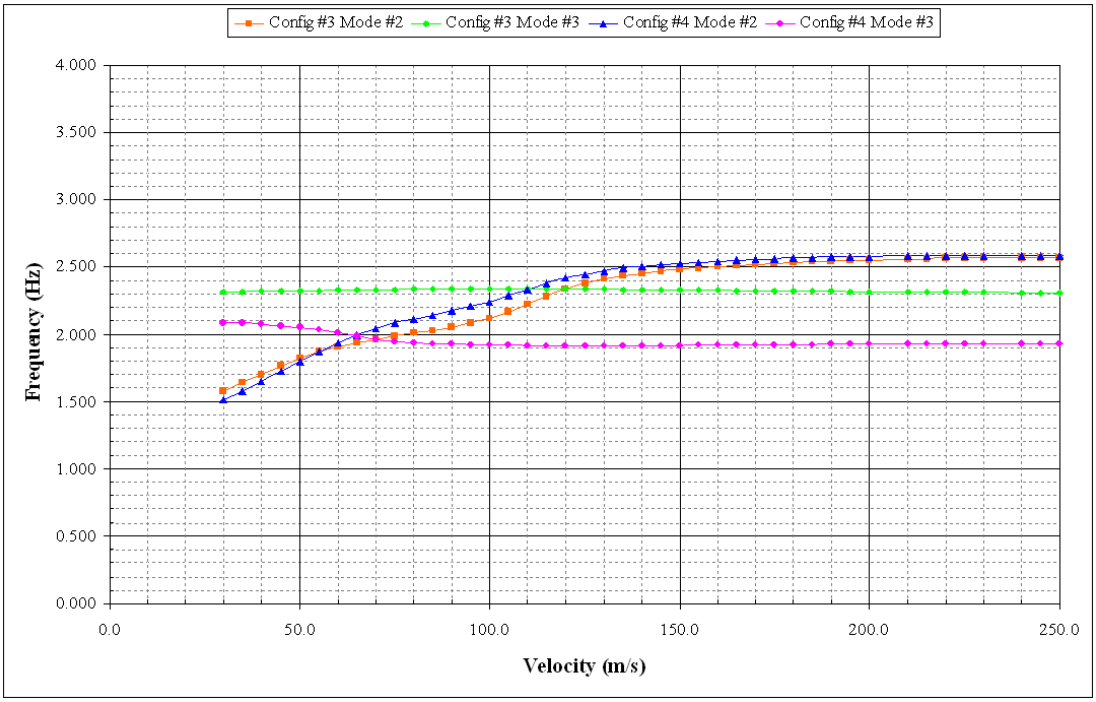

Figure 4.34 Symmetrical Flutter Velocity versus Modal Frequency

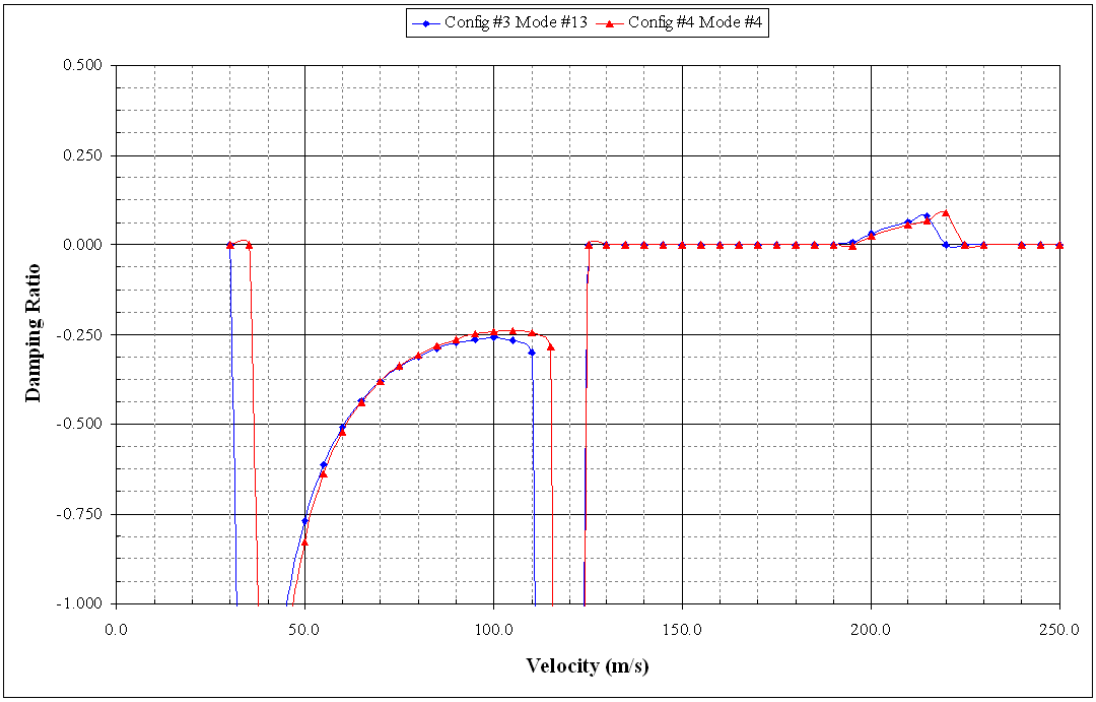

Figure 4.35 Anti-symmterical Flutter Velocity versus Modal Damping Ratio

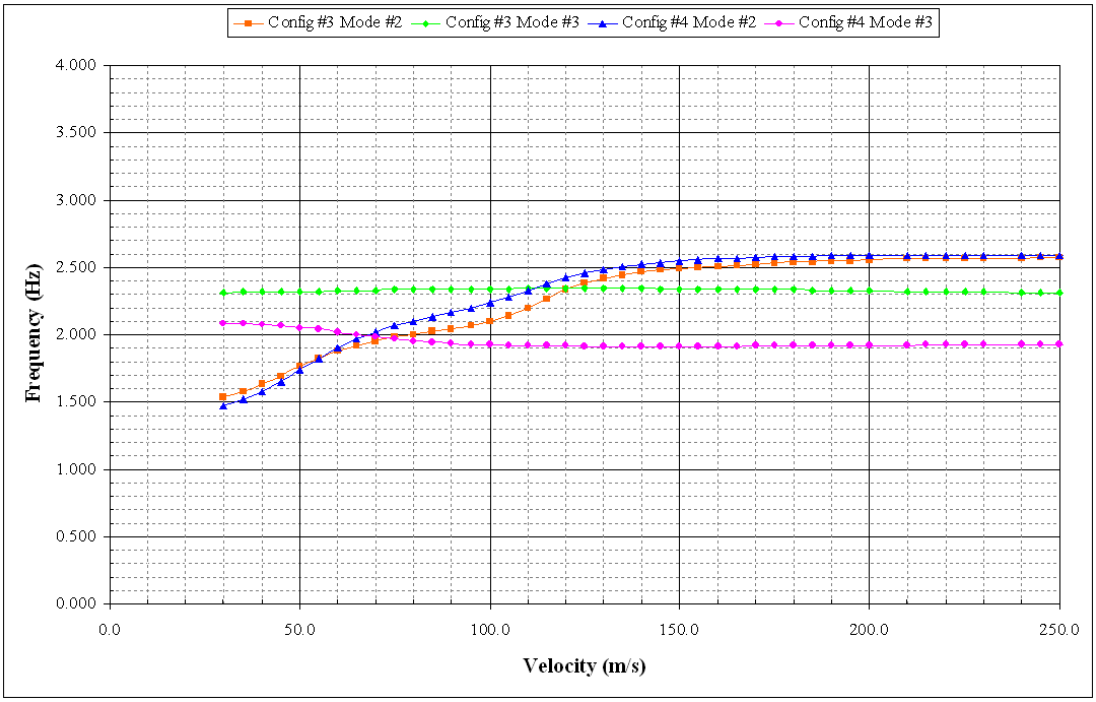

Figure 4.36 Anti-symmetrical Flutter Velocity versus Modal Frequency

As can be seen in the figures above, the flutter crossing point in the velocity-damping charts is moved to right by the addition of the slit. This shows that the flutter speed is increased due to the addition of the slit. Without the slit, the flutter speed was approximately 191 m/s (627 ft/s or 427 mph); whereas, the flutter speed with the slit was 195 m/s (640 ft/s or 436 mph). The velocity-frequency graphs show the primary two modes contributing to the flutter. The first mode (Mode #2) doesn't change very significantly in either case due to the slit. Mode #3, however, does change significantly, being reduced in both flutter cases by approximately 0.4 Hz. This reduction in frequency helps to postpone the onset of flutter.

V. Conclusions and Recommendations

5.1 Conclusions

This investigation of the joined wing examined the effects of several design parameters, providing many insights into the capability of using wing twist as a control mechanism. Initially, the effects of the ply orientations of the carbon fiber plies of the CLAS were studied. Next, the introduction of a spanwise slit into the aft wing structure was compared against configurations without the slit. Magnitudes and distributions for strain, buckling, twist and various forces and displacements were calculated in order to make these comparisons. Many useful aspects of the behavior of the slit concept in a realistic structural application were thus obtained.

The effects of the CLAS ply orientations was very small. Typically only around 25% more twist could be developed on the baseline configuration. The addition of the slit produced four and a half times the aft wing twist of the baseline, effectively masking the benefits of the ply orientations. Multiple slits allowed additional twist to be developed in the aft wing; however, the magnitude of the increases (less than 10%) are simply insufficient to warrant the added structural complexity involved.

Translations of the slit in the chordwise direction for those configurations having wing ribs in the aft wing are small enough (45 mm/1.75 in) that the slit can be restrained with the stop block concept presented. This was also true of the forces necessary to restrain the slit in the vertical direction. The maximum restraint force was only 5000 N (1100 lbs) and could easily be carried by the spar flange and stop blocks.

Since the wing studied first had already been optimized, buckling had already been taken into account. As expected, the buckling eigenvalues for the configurations with the spanwise slit were slightly lower by between 20-25% than those without a slit. Buckling and strain contours for the impact load cases showed the need for some type of load alleviation during this case. Fuel venting prior to landing is the most reasonable means of accomplishing this.

The use of a pin joint at the forward spar root caused large strains in this area. End fixity studies showed a high potential for reduction of these strains through the use of a ball joint at this location. The strains were reduced by 50% in this manner. Unfortunately, the buckling resistance was also reduced by around 50% using these different fixity conditions. This results from the loss of a substantial capacity of the aft wing in carrying the bending loads on it.

The new joint design shows strains and deformations almost identical to that of the original joint design. Analysis of the results indicate in several instances, primarily buckling and actuator forces, that this configuration is much stiffer than the original joint design. Since this new wing has not been optimized, there is a high probability that additional improvements could be realized via further structural optimization with this type of layout.

Although a major error was discovered in the setup of the analyses, initial results from the corrected models show that the relatively large strains resulting from the twisting of the aft wing are actually not as great as they originally appeared. Instead of being nearly twice the magnitude of the aerodynamic loads, the true results show that the twist strains are on the same order as the aerodynamic loads.

The flutter analysis revealed that the addition of the slit helped alleviate the onset of flutter. Since the slit helped move the vibration frequencies of the primary structural modes farther apart, the resulting flutter speed increased from 191 m/s (Mach 0.56) to 195 m/s (Mach 0.57).

The final conclusion to be drawn is that the slit concept is very much a realizable concept. Configuration #4 is the best candidate according to this research. Combining the baseline joined wing SensorCraft with a spanwise slit, CLAS composed of primarily 0° plies and a sufficiently sized actuator, this concept could take to the skies.

5.2 Recommendations

There are several areas where this investigation could be furthered. First, new optimizations of the original joined wing with the slit incorporated and the new joined wing design should be conducted. This would allow a more meaningful comparison between the different joint designs.

Second, the FEM had numerous rod elements in the forward and outboard wings that connected the upper and lower wing skins together. Their original purpose was to help alleviate local panel buckling from appearing as much in the buckling analyses. In the future these elements should be eliminated. Instead, the laminated elements making up the wing skins should be modified in such a way as to account for the separation of the major plies due to the core material. The author feels the newer NASTRAN versions already have some of this capability in the NOCOMPS parameter [23].

Also, beam elements should be used to model the spar caps. This would provide the analyst with a greater degree of control over the material distributions during another optimization. Some use could also be made of the corner thickness capability of the CQUAD4 elements, again providing an additional layer of control to the analyst.

Beam elements should also be added to the unattached edge of the aft wing ribs to provide the ribs with some means of resisting buckling. The fact none were present during this evaluation produced large numbers of low buckling eigenvalues corresponding to local rib buckling.

Finally, the aft wing root is an area which could be improved upon. During this investigation, no elements were used to form any type of closure rib in this area. Doing so would undoubtedly reduce some of the high strains seen in this area by distributing the actuator load more evenly around the root. This would be especially true near the forward spar root, which was a consistent area of high strain/stress.

Appendix A. Aft Wing Spar and Rib Locations

The aft wing section is developed from the LRN-1015 airfoil and has a constant chord of 2.5 m (8.2 ft). The wing spans approximately 21.7 m (71.2 ft) from root to joint. The forward and aft spars are located at 10% and 80% of the chord length. Figure A.1 shows some of the important dimensions of the wing cross-section.

Wing ribs were stationed at 13 evenly spaced intervals along the span of the aft wing. Table A.1 provides a listing of the rib locations, from root to joint, as a percentage of total aft wing span.

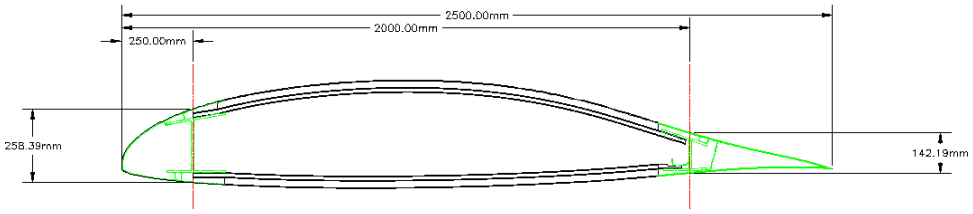

Figure A.1 Major Dimensions of Aft Wing Cross-Section

Table A.1 Aft Wing Rib Locations

Rib Number	Location (percent of span)
1	5.00
2	10.00
3	18.33
4	26.67
5	35.00
6	43.33
7	51.67
8	60.00

Table A.1 (Continued) Aft Wing Rib Locations

Rib Number	Location (percent of span)
9	68.33
10	76.67
11	85.00
12	93.33
13	98.33

Bibliography

1. Allen, D.H. and W.E. Haisler. *Introduction to Aerospace Structural Analysis*. Los Angeles: John Wiley and Sons, Inc., 1985.

2. Baker, A.A. and B.C. Hoskin. *Composite Materials for Aircraft Structures*. New York: American Institute of Aeronautics and Astronautics, Inc., 1986.

3. Ball, R.E. *The Fundamentals of Aircraft Combat Survivability Analysis and Design* (2nd Edition). Reston VA: American Institute of Aeronautics and Astronautics, Inc., 2003.

4. Blair, M. and R.A. Canfield. "A Joined-Wing Structural Weight Modeling Study," AIAA Paper 2002-1337. 43d AIAA/ASME/ASCE/AHS/ASC Structures, Structural Dynamics and Materials Conference, Denver CO, 22-25 April 2002.

5. Boeing Training and Development. *Boeing 747-400 Reference Guide*. Seattle WA: Boeing Commercial Airplane Company, March 1989.

6. Cesnik, C.E.S. and E.L. Brown. "Active Warping Control of a Joined-Wing Airplane Configuration," AIAA Paper 2003-1715. 44th AIAA/ASME/ASCE/AHS Structures, Structural Dynamics and Materials Conference, Norfolk VA, 7-10 April 2003.

7. Clarke, R., M.J. Allen, R.P. Dibley, et al. "Flight Test of the F/A-18 Active Aeroelastic Wing Airplane", AIAA Paper 2005-6316. AIAA Atmospheric Flight Mechanics Conference and Exhibit, San Francisco CA, 15-18 August 2005.

8. Cook, R.D., D.S. Malkus, M.E. Plesha, and R.J. Witt. *Concepts and Applications of Finite Element Analysis* (4th Edition). Hoboken NJ: John Wiley and Sons, Inc., 2002.

9. Etkin, B. and L.D. Reid. *Dynamics of Flight: Stability and Control*. New York: John Wiley and Sons, Inc., 1996.

10. Gallman, J.W. and I.L. Kroo. "Structural Optimization for Joined-Wing Synthesis," *Journal of Aircraft*, *33*(1): 214-223 (January/February 1996).

11. Gallman, J.W., I.M. Kroo, and S.C. Smith. "Design Synthesis and Optimization of Joined-Wing Transports," AIAA Paper 1990-3197. AIAA/ASME/ASEE Aircraft Design, Systems and Operations Conference, Dayton OH, 17-19 September 1990.

12. Gallman, J.W., I.M. Kroo, and S.C. Smith. "Optimization of Joined-Wing Aircraft," *Journal of Aircraft*, *30*(6): 897-905 (November/December 1993).

13. Hahn, H.T. and S.W. Tsai. *Introduction to Composite Materials*. Westport CT: TECHNOMIC Publishing Company, Inc., 1980.

14. Hexcel Corporation. "Datasheets and Brochures." Online database. n. pag. http://www.hexcel.com/Products/Downloads/Prepreg%20Data%20Sheets/. 10 November 2005.

15. Kaloyanova, V.B., K.N. Ghia, and U. Ghia. "Structural Modeling and Optimization of the Joined Wing of a High-Altitude Long Endurance (HALE) Aircraft," AIAA Paper 2005-1087. 43rd AIAA Aerospace Sciences Meeting and Exhibit, Reno NV, 10-13 January 2005.

16. Kroo, I.M., J.W. Gallman, and S.C. Smith. "Aerodynamic and Structural Studies of Joined-Wing Aircraft," *Journal of Aircraft*, *28*(1): 74-81 (January 1991).

17. Lin, H.H., J. Jhou, and R. Stearman. "Influence of Joint Fixity on the Aeroelastic Characteristics of a Joined Wing Structure," AIAA Paper 1990-0980. 31st AIAA/ASME/ASCE/AHS/ASC Structures, Structural Dynamics and Materials Conference, Long Beach CA, April 1990.

18. Livne, E. "Aeroelasticity of Joined-Wing Airplane Configurations: Past Work and Future Challenges - A Survey," AIAA Paper 2001-1370. 42d AIAA/ASME/ASCE/AHS/ASC Structures, Structural Dynamics and Materials Conference, Seattle WA, 16-19 April 2001.

19. Lokos, W.A., C.D. Olney, N.D. Crawford, et al. "Wing Torsional Stiffness Tests of the Active Aeroelastic Wing F/A-18 Airplane," AIAA Paper 2002-1333. 43rd AIAA/ASME/ASCE/AHS Structures, Structural Dynamics and Materials Conference, Denver CO, 22-25 April 2002.

20. Lucia, D.J. "The SensorCraft Configurations: A Non-Linear AeroServoElastic Challenge for Aviation," AIAA Paper 2005-1943. 46th AIAA/ASME/ASCE/AHS/ASC Structures, Structural Dynamics and Materials Conference, Austin TX, 18-21 April 2005.

21. Manning, Charles W. Air Combat Command, F-15 Fighter Maintenance Liaison, 330th Fighter Sustainment Group, Robins AFB, GA. Electronic Correspondence. 2056Z, 1 January 2006.

22. "MATLAB 7 Student Version, Release 14," The MathWorks, Inc., 2004.

23. MSC Software Corp. *MSC.NASTRAN 2004 Quick Reference Guide*. Santa Ana CA: MacNeal-Schwendler Corp., 2003.

24. MSC Software Corp. *MSC/PATRAN Version 8 User's Guide*. Los Angeles: MacNeal-Schwendler Corp., September 1998.

25. Niu, M.C. *Airframe Structural Design*. Hong Kong: Conmilit Press Ltd., 1988.

26. Northrop Grumman Corporation. *SensorCraft Low Band Conformal Load Bearing Antenna Structures (S-CLAS): R & D Status Report No. 13*. Contract F33615-00-D-3054, August 2002.

27. O'Bannion, J., J. Jhou, and R. Stearman. *A Study of Joint Fixativity in a Joined-Wing Aircraft*. NASA Technical Memorandum 112388, March 1987.

28. Pendleton, E., M. Lee, and L. Wasserman. "Application of Active Flexible Wing Technology to the Agile Falcon," *Journal of Aircraft*, *29*(3): 444-451 (May-June 1992).

29. Perry III, B., S.R. Cole, and G.D. Miller. "Summary of an Active Flexible Wing Program," *Journal of Aircraft*, *32*(1): 10-15 (January-February 1995).

30. Peters, S.T. (ed.). *Handbook of Composites* (2nd Edition). New York: Chapman and Hall, 1998.

31. Rasmussen, C.C., M. Blair, and R.A. Canfield. "Joined-Wing Sensor-Craft Configuration Design," AIAA Paper 2004-1760. 45th AIAA/ASME/ASCE/AHS Structures, Structural Dynamics and Materials Conference, Palm Springs CA, 19-22 April 2004.

32. Rasmussen C.C., R.A. Canfield, and Blair, M. "Optimization Process for Configuration of Flexible Joined-Wing," AIAA Paper 2004-4330. 10th AIAA/ISSMO Multidisciplinary Analysis and Optimization Conference, Albany NY, 30 August - 01 September 2004.

33. Reich, G.W., J.C. Bowman, and B. Sanders. "Large-Area Aerodynamic Control for High-Altitude Long-Endurance Sensor Platforms," *Journal of Aircraft*, *42*(1): 237-244 (January-February 2005).

34. Reich, G.W., D.E. Raveh, and P.S. Zink. "Application of Active-Aeroelastic-Wing Technology to a Joined-Wing SensorCraft," *Journal of Aircraft*, *41*(3): 594-602 (May-June 2004).

35. Roberts, R.W., M. Blair, and R.A. Canfield. "Joined-Wing Aeroelastic Design with Geometric Nonlinearity," *Journal of Aircraft*, *42*(4): 832-848 (July/August 2005).

36. Roberts, R.W., M. Blair, and R.A. Canfield. "Sensor-Craft Structural Optimization and Analytical Certification," AIAA Paper 2003-1458. 44th AIAA/ASME/ASCE/ AHS Structures, Structural Dynamics and Materials Conference, Norfolk VA, 7-10 April 2003.

37. Saada, A.S. *Elasticity Theory and Applications* (2nd Edition). Malabar FL: Krieger Publishing Co., 1993.

38. Samuels, M.F. "Structural Weight Comparison of a Joined Wing and a Conventional Wing," *Journal of Aircraft*, *19*(6): 485-491 (June 1982).

39. Sang, L. *MSC/NASTRAN Handbook for Nonlinear Analysis*. Los Angeles: MacNeal-Schwendler Corp., 1992.

40. Schwartz J., R.A. Canfield, and Blair, M. "Aero-Structural Coupling and Sensitivity of a Joined-Wing SensorCraft," AIAA Paper 2003-1580. 44th AIAA/ASME/ASCE/ AHS Structures, Structural Dynamics and Materials Conference, Norfolk VA, 7-10 April 2003.

41. Seely, F.B. and J.O. Smith. *Advanced Mechanics of Materials* (2nd Edition). New York: John Wiley and Sons, October 1963.

42. Smallwood, B.P., R.A. Canfield, and A.J. Terzuoli, Jr. "Structurally Integrated Antennas on a Joined-Wing Aircraft," AIAA Paper 2003-1459. 44th AIAA/ASME/ ASCE/AHS Structures, Structural Dynamics and Materials Conference, Norfolk VA, 7-10 April 2003.

43. Touchstone Research Laboratory, Ltd. "Product Data Sheet: CFOAM® Carbon Foams," Website. http://www.cfoam.com/pdf/CFOAMProductDataSheet.pdf. 10 November 2005.

44. Wolkovitch, J. "Joined Wing Aircraft," U.S. Patent 3,942,747, 09 March 1976.

45. Wolkovitch, J. "Joined Wing Aircraft," U.S. Patent 4,365,773, 28 December 1982.

46. Wolkovitch, J. "The Joined Wing: An Overview," *Journal of Aircraft*, *23*(3): 161-178 (March 1986).

47. Zona Technolgy, Inc. *ZAERO 7.1 User's Manual*. Scottsdale, AZ: Zona Technology, Inc., September 2004.

Vita

Captain Fred A. Kimler III graduated from Early County High School in Blakely, GA. He entered undergraduate studies at Embry-Riddle Aeronautical University in Dayton Beach, FL, graduating with a Bachelor of Science degree in Aerospace Engineering in December of 1996. He worked as an interiors engineer for various companies prior to receiving his commission through Officer Training School at Maxwell AFB, AL in May of 2001.

His first assignment was to Robins AFB, GA as an F-15 Flight Equipment Engineer. He also received training as an Aircraft Battle Damage Repair Engineer and deployed to Qatar in this capacity in support of Operation IRAQI FREEDOM. In March of 2004, he entered the Graduate School of Engineering and Management, Air Force Institute of Technology. Upon graduation, he will be assigned to the Air Force Research Laboratory's Propulsion Division at Wright-Patterson AFB, OH.

REPORT DOCUMENTATION PAGE

Form Approved
OMB No. 074-0188

PLEASE DO NOT RETURN YOUR FORM TO THE ABOVE ADDRESS.

1. REPORT DATE *(DD-MM-YYYY)*	**2. REPORT TYPE**	**3. DATES COVERED** *(From – To)*
23-03-2006	**Master's Thesis**	May 2004 – Mar 2006

TITLE AND SUBTITLE

Structural Design of Wing Twist for Pitch Control of Joined Wing SensorCraft

5a. CONTRACT NUMBER

5b. GRANT NUMBER

5c. PROGRAM ELEMENT NUMBER

AUTHOR(S)

Kimler, Fred A., Captain, USAF

5d. PROJECT NUMBER

5e. TASK NUMBER

5f. WORK UNIT NUMBER

7. PERFORMING ORGANIZATION NAMES(S) AND ADDRESS(S)

Air Force Institute of Technology
Graduate School of Engineering and Management (AFIT/ENY)
2950 Hobson Way
WPAFB OH 45433-7765

8. PERFORMING ORGANIZATION REPORT NUMBER

AFIT/GAE/ENY/06-M20

9. SPONSORING/MONITORING AGENCY NAME(S) AND ADDRESS(ES)

AFRL/VAS
Attn: Dr. Maxwell Blair
Air Vehicles Directorate
WPAFB OH 45433-7542 DSN: 785-8430

10. SPONSOR/MONITOR'S ACRONYM(S)

11. SPONSOR/MONITOR'S REPORT NUMBER(S)

12. DISTRIBUTION/AVAILABILITY STATEMENT

APPROVED FOR PUBLIC RELEASE; DISTRIBUTION UNLIMITED.

13. SUPPLEMENTARY NOTES

14. ABSTRACT

This research investigated two aspects of the aft wing structure of a joined wing SensorCraft. First, the efficacy of a novel approach for incorporating wing twist for pitch control was analyzed. This design involved adding a spanwise sliding joint into the wing structure at the lower aft spar of the vehicle's aft wing. Second, the joint section where the forward and aft wings connect and form the outboard wing was redesigned and analyzed to improve the load transmission between the wing spars. Using MSC.NASTRAN, linear and non-linear static analyses were performed to examine the efficiency of the wing twist sliding joint and the forces required to achieve sufficient angular deflections for control. MSC.Patran was then used to perform post-processing of the raw data. Several variations of sliding joint location and composite ply angles were conducted. The sliding joint produced marked improvement in angular deflection over the baseline configuration. Surprisingly, however, ply angle did not have a large effect on the resulting deflections. Additional sliding joints incorporated into the wing structure produced no notable improvements in the obtained deflections either. Although the strain induced into the structure by the aft wing twist was on the order of the aerodynamic forces alone, the force required to twist the wing was significantly reduced by adding the slit in all cases. Flutter speed did not differ notably by the addition of the slit into the aft wing, yet some reduction in buckling strength was noted. The redesigned joint planform does appear to recover some of the buckling resistance lost due to the slit.

15. SUBJECT TERMS

Joined Wing, SensorCraft, Wing Twist

16. SECURITY CLASSIFICATION OF: Unclassified			**17. LIMITATION OF ABSTRACT**	**18. NUMBER OF PAGES**	**19a. NAME OF RESPONSIBLE PERSON**
REPORT	**ABSTRACT**	**c. THIS PAGE**			Dr. Robert Canfield (ENY)
U	**U**	**U**	**UU**	**117**	**19b. TELEPHONE NUMBER** *(Include area code)* (937) 436-3069 e-mail: Robert.Canfield@afit.edu

Standard Form 298 (Rev: 8-98)
Prescribed by ANSI Std. Z39-18